Quaternary Science Reviews 358 (2025) 109307

Contents lists available at ScienceDirect

Quaternary Science Reviews

journal homepage: www.elsevier.com/locate/quascirev

Sensitivity to climate and vegetation dynamics of a peatland record from central Cameroon during the African Humid Period

Valentine Schaaff [a,*], Vincent Grossi [a,b], Matthew Makou [a], Yannick Garcin [c], Pierre Deschamps [c], Bruno Hamelin [c], Christopher A. Kiahtipes [d], David Sebag [e], Benjamin Ngounou Ngatcha [f], Guillemette Ménot [a]

[a] ENS Lyon, UCBL, CNRS, UMR 5276 LGL-TPE, Lyon, France
[b] Aix Marseille Univ, CNRS, Université de Toulon, IRD, Mediterranean Institute of Oceanography (MIO), Marseille, France
[c] Aix Marseille Univ, CNRS, IRD, INRAE, CEREGE, Aix-en-Provence, France
[d] University of South Florida, Tampa, United States
[e] IFP Energies Nouvelles, Earth Sciences and Environmental Technologies Division, Rueil-Malmaison, France
[f] Department of Earth Sciences, Faculty of Sciences, University of Ngaoundéré, Ngaoundéré, Cameroon

ARTICLE INFO

Handling editor: Yan Zhao

Keywords:
Lipid biomarkers
Pollen
Central Africa (Cameroon)
African Humid Period
Tropical peatland
Isotopes

ABSTRACT

Significant climatic and vegetation changes have occurred in tropical Africa over the Holocene, especially during the African Humid Period (AHP). However, the complexity of interpreting and comparing several proxies from diverse sites complicates the characterization and differentiation of climatic and environmental changes at local, regional and global scales. This study investigates a 6-m peat core from the Ngaoundaba maar volcanic crater (Northeastern Cameroon, later simply called Ngaoundaba), spanning the last 10 ka using pollen analysis and a large panel of lipid biomarkers. We produce new high-resolution, continuous, multiproxy records of vegetation, temperature, and precipitation spanning most of the Holocene. All of these proxies indicate a substantial transition approximately 5.7–5.6 ka cal BP, which is supported by cluster analyses and marks the end of the AHP. A shift from an open-water to a vegetated peatland, the disappearance of some wooded species, and the expansion of grass and sedge pollen all indicate significant local and regional changes. The gradual terrestrialization of peat surfaces also had an impact on lipid biomarker proxies. An unusual extensive variation in hydrogen isotopic composition (D/H) of long-chain *n*-alkanes during the Holocene, in contrast to other records from West and Central Africa, may be attributed to the increased contribution from local wetland plants, including sedges and grasses, which thrive in peat water that is more D-enriched than rainwater, peat water being the water accumulating in the wetland. Likewise, temperature variations reconstructed using bacterial branched glycerol dialkyl glycerol tetraethers (brGDGTs) are influenced by confounding factors, like changes in peat pH or moisture levels, which may be constrained using our multiproxy methodology. The temperature record from Ngaoundaba indicates a slight increase in temperature during the mid-Holocene relative to pre-industrial levels. The Ngaoundaba peat deposit documents a massive and abrupt shift in vegetation at the end of the AHP, linked with changes in precipitation amount and/or seasonality, which also significantly affected the peat microbial community. The Ngaoundaba peat record, because of its high sensitivity to climatic and environmental changes, is a crucial new source for understanding the end of the African Humid Period in Western Central Africa.

1. Introduction

Precipitation has long been recognized in tropical and equatorial Africa as a critical climatic component influencing vegetation zonation and having a significant influence on human communities (Pausata et al., 2020). During the early Holocene, the region experienced a northward and southward shift in vegetation zones, driven by changes in the amount and seasonality of precipitation (e.g., DeMenocal et al., 2000; Salzmann et al., 2002; Shanahan et al., 2015). This period, referred to as the African Humid Period (AHP), peaked between 9000 and 6000 years ago, and has since been extensively studied. A comprehensive array of proxies has been employed to reconstruct the

* Corresponding author.
E-mail address: valentine.schaaff@ens-lyon.fr (V. Schaaff).

https://doi.org/10.1016/j.quascirev.2025.109307
Received 14 November 2024; Received in revised form 25 February 2025; Accepted 8 March 2025
Available online 11 April 2025
0277-3791/© 2025 The Authors. Published by Elsevier Ltd. This is an open access article under the CC BY-NC license (http://creativecommons.org/licenses/by-nc/4.0/).

end of the African Humid Period, including windborne dust via terrigenous input (DeMenocal et al., 2000), upwelling intensity through excess ^{230}Th (Adkins et al., 2006), pollen analyses (e.g., Vincens et al., 2010; Lézine, 2017), temperature and precipitation reconstructions based on lipid biomarkers (e.g., Berke et al., 2012; Shanahan et al., 2015), and fossil diatoms (Yacoub et al., 2023), among others. Published data, including marine and terrestrial environments across diverse ecological conditions, have highlighted the intricacy of climatic and environmental responses toward the end of the AHP and the timing and abruptness of its termination are still subject to debate.

In Western Central Africa, hydroclimatic reconstructions, based on the hydrogen isotopic composition (D/H or δD) of plant wax-derived *n*-alkanes, demonstrate differing patterns throughout the Holocene (Collins et al., 2017; Garcin et al., 2018, 2022; Niedermeyer et al., 2010; Schefuβ et al., 2005; Shanahan et al., 2015; Tierney et al., 2017). Shanahan et al. (2015) emphasized the intricate spatial and temporal dynamics of the termination of the African Humid Period (AHP), suggesting a time-transgressive end of the AHP marked by an abrupt local termination that occurred later at lower latitudes. Nonetheless, the δD record from the lake Barombi closely aligns with insolation variations, suggesting a progressive termination of the AHP (Garcin et al., 2018). Vegetation reconstructions derived from pollen analyses reveal a significant response to climate change at the end of the AHP, although the timing and magnitude of these responses differed across various regions (e.g., Vincens et al., 2010; Lézine et al., 2021).

Modeling studies further illustrated the intricate nature of precipitation alterations at the end of the AHP, emphasizing significant feedback mechanisms from vegetation, land-surface, and ocean-surface interactions on the monsoon regime, alongside non-monsoon dynamics such as extratropical troughs (e.g., Kutzbach et al., 1996; Claussen et al., 1999; Renssen et al., 2006). Recent transient models effectively represent the temporally transgressive end of the AHP (e.g., Kutzbach et al., 1996; Claussen et al., 1999; Renssen et al., 2006; Dallmeyer et al., 2020). Regionally, climatic simulations utilizing several Global Climate Models (GCMs) exhibit considerable variances in the timing of the AHP, leading to substantial variations in the projected alterations in vegetation (Hély et al., 2009). Although insolation forcing is the primary factor triggering the end of the AHP, the intricate and diverse climatic feedbacks, together with regional and local influences on environmental change, complicate the comprehension of the AHP termination and hinder the comparison of data from various sites.

The scarcity of multiproxy records complicates the establishment of links between proxies and their responses to local changes, whether similar or different. Comparing proxies is essential for improving our comprehension of the AHP and refining its timing. In Western Central Africa, multiproxy records that encompass the end of the AHP and juxtapose pollen analysis with lipid biomarkers are limited to a few locations, such as Lake Barombi (Garcin et al., 2018; Giresse et al., 1994) and Lake Bosumtwi (Shanahan et al., 2006, 2015; Miller et al., 2018). However, the variable temporal resolutions of these records complicate comparisons among proxies.

This work reconstructs the dynamics of the end of the AHP utilizing lipid biomarkers (long chain *n*-alkanes and branched glycerol dialkyl glycerol tetraethers - brGDGTs) and pollen records from the Ngaoundaba peat deposit in northern Cameroon (Fig. 1). This site is situated on the Adamawa plateau within the Sudano-Guinean wooded savanna region (Letouzey, 1958). This area, situated between the open savannas of the Sahelian and Sudanian zones and the closed forests of the Guineo-Congolian rainforests, has significant promise for paleoclimatic research. Currently, records from the Adamawa plateau do not extend beyond the last 7 ka cal BP (Nguetsop et al., 2011; Vincens et al., 2010), with some exhibiting intricate or inadequately defined age models (e.g., Ngos and Giresse, 2012; Nguetsop et al., 2013). Here we present the first high-resolution record of the last 10,000 years on the Adamawa plateau, encompassing the end of the AHP, reconstructing past variations in vegetation, precipitation, and temperature using novel multi-proxy data, supplemented by previously published bulk organic data and pH reconstructions (Schaaff et al., 2023, 2024). This high-resolution, continuous paleoenvironmental and paleoclimatic record shows a major climatic change at approximately 5.7–5.6 ka cal BP. The Ngaoundaba location exhibited susceptibility to short-term climate fluctuations. Our multi-proxy approach effectively differentiates

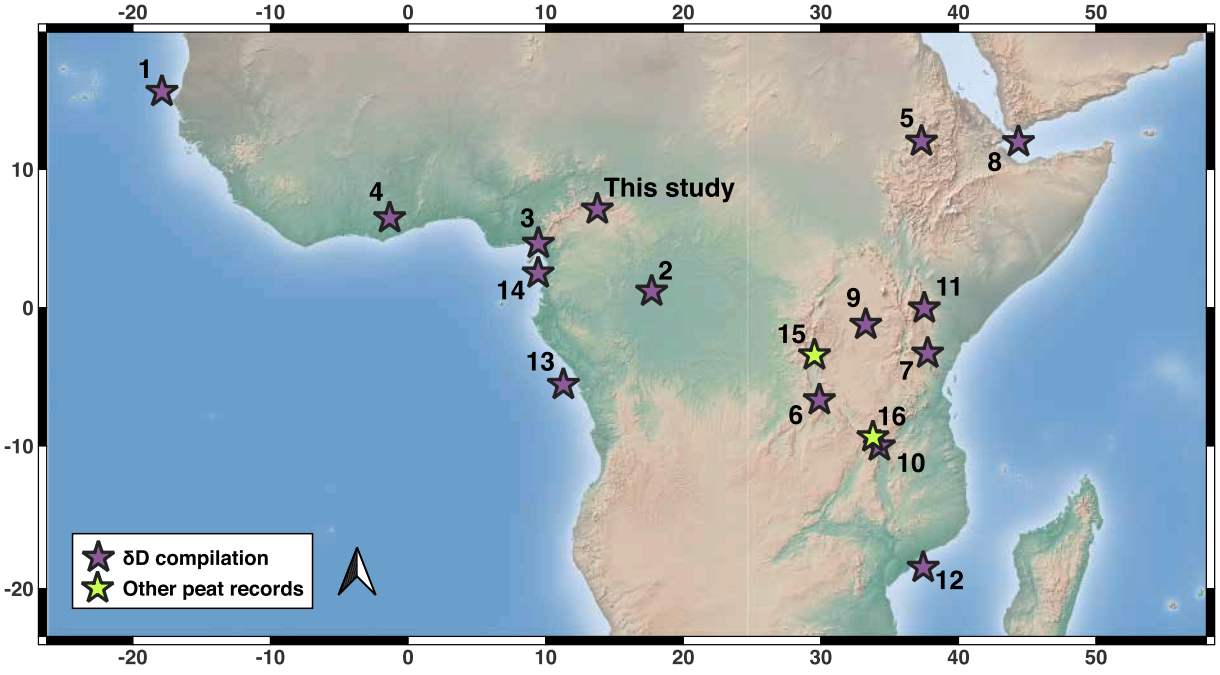

Fig. 1. Location of the Ngaoundaba peat and other paleoclimate and paleoenvironmental records in the intertropical and equatorial regions of Africa. Green and violet symbols refer to the compilation of δD records and other peat records, respectively. Site numbers refer to the associated references in Table S. 1. The present-day vegetation at each site is detailed in subsection S.2.2. (For interpretation of the references to color in this figure legend, the reader is referred to the Web version of this article.)

regional climate signals from local environmental changes, while peat records provide insights into both long- and short-term climate dynamics, as indicated by the study.

2. Material and methods

2.1. Study site and material

The Ngaoundaba peat deposit is situated in a volcanic crater on the Adamawa Plateau in Northeast Cameroon (N7.135° E13.690°, 1175 m above sea level). The current climate is characterized by two distinct seasons: a 6-month dry season from October to March and a 6-month rainy season from April to October. According to the CRU database, the current mean annual air temperature (MAAT) is 22.2 °C and the mean annual precipitation (MAP) is 1482 mm (Harris et al., 2014).

This part of the Adamawa Plateau is currently classified as Sudano-Guinean wooded savanna and is bordered to the north by Sudanian savanna-dry woodland mosaics (Letouzey, 1958; White, 1983). The Sudano-Guinean wooded savanna zone is characterized by the presence of *Daniella oliveri* (Fabaceae) and *Lophira lanceolata* (Ochnaceae) tree species (Letouzey, 1985; Vincens et al., 2010). There is a broad transition zone from 6° N to 4° N between the wooded Sudano-Guinean savannas and dry/seasonal Guineo-Congolian forests to the south. The *in situ* growing vegetation of the Ngaoundaba peat deposit is dominated by sedges (*Cyperus* sp).

Analyses are based on a 6-m-long core (named NGBA19) collected in February 2019 using a Russian peat corer. The core is composed of dark brown peat without visible sandy or clayey zones. The core was subsampled at 2.5-cm intervals. Compound-specific organic geochemical analyses were performed on 73 samples, and pollen analyses were performed on 60 samples. We previously demonstrated that the bulk organic data, notably Total Organic Carbon (TOC), were primarily controlled by the decomposition of organic matter. After removing this signal, the remaining variation can be interpreted in terms of past change in paleoclimatic conditions (Schaaff et al., 2023). Additionally, the Ngaoundaba peat deposit provides the first comparison of two pH reconstructions, one based on hopanes and the other on brGDGTs (Schaaff et al., 2024). Although the range of variations differs between the two pH reconstructions, they show similar variations reflecting the response of the microbial community to past environmental changes.

2.2. ^{14}C dating and bulk organic analyses

The age model of the Ngaoundaba peat core is based on 30 radiocarbon dates carried out at the LMC14 Laboratory (Saclay, France). Details on the dating and calibration of the age model are given in Schaaff et al. (2023). Briefly, the 6-m-long NGBA19 peat core covers the last 10 ka. The sediment accumulation rate is relatively uniform, with exceptions at depths of approximately 150 cm and 200 cm, where there is a rapid increase in age within a narrow sediment layer. Organic geochemical and pollen samples were selected at regular depth intervals. Six organic geochemical samples were added at depths of 150 and 200 cm, with three samples at each depth. The average temporal resolutions of the compound-specific organic geochemical and pollen analyses were approximately 130 and 170 years, respectively.

Bulk organic analyses are presented in detail in Schaaff et al. (2023). Briefly, for elemental and stable isotope analyses (Total Organic Carbon (TOC) and $\delta^{13}C$ composition of TOC, hereafter $\delta^{13}C_{bulk}$), samples were analyzed using an elemental analyzer (Vario ISOTOPE Select, Elementar) coupled to a thermal conductivity detector and an isotope ratio mass spectrometer (Vision, Elementar). Every 10 samples, a working standard (IVA sediment) was analyzed to normalize the mass spectrometer signal. Samples were analyzed for Rock Eval® thermal analyses (Hydrogen Index, HI), using a Rock-Eval® 6 (Vinci Technologies, France).

2.3. Compound-specific organic geochemical analyses

2.3.1. Sample preparation

All samples were freeze-dried, ground and homogenized. Lipid extraction was performed two times from 0.3 g of each sample with 10 mL dichloromethane (DCM)/methanol (3:1, *v/v*) using a MARS 6 CEM microwave extraction system. Following each extraction, the supernatant was filtered through a sintered Teflon filter. Synthetic C_{46} GDGT was added to the combined extracts of each sample as an internal standard (Huguet et al., 2006). The total lipid extract was separated by column chromatography on silica gel into three fractions of increasing polarity. A hydrocarbon fraction containing *n*-alkanes was first eluted with 8 mL of hexane. A second fraction was eluted with 5 mL hexane/DCM (1:1, *v/v*). Alcohols, including brGDGTs, were eluted in a third fraction with 10 mL DCM/methanol (1:1, *v/v*).

2.3.2. n-Alkanes analyses

2.3.2.1. Molecular analyses by gas chromatography. Copper curls activated with HCl were added to the hydrocarbon fractions to remove elemental sulfur. After a first GC-FID analysis (HP 6890 A), GC-MS analyses (Agilent 6890 N GC coupled to an Agilent 5975C MSD and Agilent 7890 B GC coupled to an Agilent 5977 B MSD) were performed for identification and quantification of the different compounds. Both GC-MS instruments provided comparable data. Integration of *n*-alkane peaks were performed using the m/z 71 ion chromatogram to limit the influence of coelution and compared with an external standard solution containing commercial pentacosane (n-C_{25}) for quantification. *n*-Alkane abundances were calculated using all alkanes from *n*-C_{19} to *n*-C_{37}.

2.3.2.2. n-Alkane ratios. The carbon preference index (CPI), which describes the relative abundance of C-odd vs C-even *n*-alkanes, was calculated for *n*-C_{25} to *n*-C_{35} homologues using the revised equation from Marzi et al. (1993) and was originally defined to characterize *n*-alkane preservation:

$$CPI = \frac{(C_{25} + C_{27} + C_{29} + C_{31} + C_{33}) + (C_{27} + C_{29} + C_{31} + C_{33} + C_{35})}{2*(C_{26} + C_{28} + C_{30} + C_{32} + C_{34})}$$

The average chain length (ACL) describes the dominant chain-length of a fixed range of odd numbered *n*-alkanes. The considered range of *n*-alkanes is usually *n*-C_{27} to *n*-C_{31} (Poynter and Eglinton, 1990), but shorter (e.g. *n*-C_{23}, *n*-C_{25}) and longer chain (e.g. *n*-C_{33}) *n*-alkanes can also be included (Poynter et al., 1989). As *n*-C_{33} *n*-alkane is an important component of long chain *n*-alkane assemblage, we chose the following equation for ACL calculation:

$$ACL_{27-33} = \frac{(27*C_{27} + 29*C_{29} + 31*C_{31} + 33*C_{33})}{(C_{27} + C_{29} + C_{31} + C_{33})}$$

The P_{aq} ratio was calculated using the equation from Ficken et al. (2000) based on lacustrine vegetation:

$$P_{aq} = \frac{(C_{23} + C_{25})}{(C_{23} + C_{25} + C_{29} + C_{31})}$$

The P_{aq} ratio has been reinterpreted in *Sphagnum* peat as a proxy for the contribution of *Sphagnum* mosses compared to other peat-forming plants (Nichols et al., 2006). Since *Sphagnum* mosses are absent from the Ngaoundaba peat deposit, we use the P_{aq} ratio as a proxy for the contribution of submerged versus emerged macrophytes (Ficken et al., 2000).

2.3.2.3. Compound-specific isotope analyses. Prior to carbon and hydrogen isotopic measurements, the hydrocarbon fractions were separated into a saturated and an unsaturated fraction by column chromatography using silica gel impregnated with $AgNO_3$ (10 % wt). Saturated fractions containing *n*-alkanes were eluted with 3–4 mL of *n*-

heptane. Unsaturated fractions were eluted with 3–4 mL of ethyl acetate. Carbon isotopic compositions were measured at the LGL-TPE (Université Claude Bernard Lyon 1) using an Agilent 7890 B GC coupled to an Isoprime visION Isotope Ratio Mass Spectrometer via an Isoprime GC-5 combustion interface (Elementar). The GC-5 furnace was operated at 850 °C. An autotune and tests of stability and linearity of the signal were performed daily using the software ionOS. Stable carbon isotopic compositions (expressed as $\delta^{13}C$ values) were calibrated using a reference CO_2 gas reported to VPDB scale. Two Mix hydrocarbon B4 standards (A Schimmelmann, Indiana University) were measured every 4 to 5 samples and used to correct the $\delta^{13}C$ values. Samples were analyzed in duplicates. For δD measurements, the GC-5 pyrolysis furnace was operated at 1450 °C. Daily autotune, H_3+ correction and test of stability were performed using the software ionOS. The mean value of the H_3+ was 3.708 (n = 26, stdev = 0.655). δD values were calibrated using the reference H_2 gas reported to VSMOW. Each week, the pyrolysis furnace was conditioned five times with 1 µL hexane prior to any analysis and a series of 8 Mix B4 measurements was performed and used for data correction. In addition, one Mix B4 measurement was analyzed every 4 to 5 injections to assure the limited impact of drift. Samples were analyzed in duplicates. Mean standard deviations calculated as $2^{*}\Delta/\sqrt{2}$ with Δ, the difference between the duplicate measures. Mean δD standard deviations are 4.8, 5.4 and 5.9 ‰ for *n*-C_{29}, *n*-C_{31} and *n*-C_{33}, respectively. Mean $\delta^{13}C$ standard deviations are 0.3 ‰ for *n*-C_{29}, *n*-C_{31} and *n*-C_{33}.

2.3.2.4. Correction of carbon and hydrogen isotope values.

- *Correction of* $\delta^{13}C$ for *Suess effect*

Anthropogenic activities such as fossil fuel combustion lead to changes in atmospheric concentration and isotopic ratio of ^{13}C and ^{14}C, known as the Suess effect, which must be taken into account prior to interpretation (e.g., Keeling, 1979). This effect is significant since the 1860s (Francey et al., 1999) and is calculated as the difference between atmospheric $\delta^{13}C$ at the age of the sample and the value of pre-industrial atmospheric $\delta^{13}C$ (−6.4‰) measured using tree-ring samples (McCarroll and Loader, 2004); it can also be estimated using CO_2 extracted from ice cores (Rubino et al., 2013).

- *Correction of δD for vegetation change*

We used paired $\delta^{13}C_{n\text{-alk}}$ to correct $\delta D_{n\text{-alk}}$, following the previous approach used in similar contexts (e.g., Shanahan et al., 2015; Garcin et al., 2018). This accounted for changes in hydrogen fractionation factors of vegetation types and photosynthetic pathways. The relative contribution of C_3 plant waxes (f_{C3}) to the sediment is assessed by using the linear binary mixing model as follows:

$$\delta^{13}C_{n-alk} = f_{C3}\delta^{13}C_{C3} + (1 - f_{C3})\delta^{13}C_{C4}$$

$$f_{C3} = \frac{\delta^{13}C_{n-alk} - \delta^{13}C_{C4}}{\delta^{13}C_{C3} - \delta^{13}C_{C4}}$$

The end-member values for C_3 plants ($\delta^{13}C_{C3} = -33.4$‰ for *n*-$C_{29}$, $\delta^{13}C_{C3} = -33.8$‰ for *n*-$C_{31}$ and $\delta^{13}C_{C3} = -34$‰ for *n*-C_{33}) and C_4 plants ($\delta^{13}C_{C3} = -19.8$‰ for *n*-$C_{29}$ and $\delta^{13}C_{C4} = -20.1$‰ for *n*-$C_{31}$ and *n*-C_{33}) are taken from Garcin et al. (2014) and are based on an African plant dataset compiling several studies (Rommerskirchen et al., 2006; Vogts et al., 2009; Kristen et al., 2010; Garcin et al., 2014).

The influence of vegetation on $\delta D_{n\text{-}C31}$ can be associated with a difference in apparent fractionation ε between precipitation and *n*-alkane for C_3 plants (−129‰) on the one hand and C_4 plants (−145‰) on the other hand (Smith and Freeman, 2006; Feakins et al., 2016). Using the previously calculated f_{C3}, we estimated the ε_{corr} of each sample as follows:

$$\varepsilon_{corr} = f_{C3}\varepsilon_{C3} + (1 - f_{C3})\varepsilon_{C4}$$

in a last step, we used ε_{corr} to correct $\delta D_{n\text{-alk}}$ and obtain $\delta D_{n\text{-alk-corr}}$:

$$\delta D_{n-alk-corr} = \left[\frac{\delta D_{n-alk} + 1000}{\left(\frac{\varepsilon_{corr}}{1000}\right) + 1}\right] - 1000$$

2.3.3. brGDGT analyses

Fractions containing brGDGTs were filtered using 0.45 µm PTFE filters. brGDGT analyses were performed using High Performance Liquid Chromatography Mass Spectrometry (HPLC-APCI-MS, Agilent 1200) at the LGL-TPE (ENS de Lyon). Separation was achieved on two silica columns in series (ACQUITY UPLC BEH HILIC, WATERS) following the procedure of Hopmans et al. (2016) slightly modified (i.e. using hexane/isopropanol (98.2:1.8, *v/v*)). Peaks corresponding to brGDGTs were manually integrated and quantified using the peak area of C_{46}. The selected m/z values are 743.9, 1050.2, 1048.2, 1046.2, 1036.2, 1034.2, 1032.2, 1022.2, 1020.2, and 1018.2.

We tested 4 different temperature calibrations (Table 1). Comparison of the four calibrations is presented in the supplementary material. Three of them use the Methylation of Branched Tetraethers ratio defined by De Jonge et al. (2014) (MBT'_{5Me}) to reconstruct past changes in temperature:

$$MBT'_{5Me} = \frac{Ia + Ib + Ic}{Ia + Ib + Ic + IIa + IIb + IIc + IIIa}$$

2.4. Pollen analyses

2.4.1. Sample preparation

Pollen analyses were carried out at IASCE paleoecology laboratory at the University of South Florida. Samples were weighed, and their volume was estimated using displacement. Two tablets of *Lycopodium* sp. spores were added to each sample (Batch #100320201) and dissolved with 10 % Hydrochloric acid (HCl). Samples were centrifuged, decanted, and rinsed until pH neutral, then fine materials were isolated using gravity separation and screening through 250 µm sieves. Because these samples were organic with little mineral content, we omitted treatment with Hydrofluoric acid. The organic fraction was digested through a 10-min hot bath in a 10 % Potassium Hydroxide solution at 80 °C. Samples were then centrifuged, the solution was decanted, and a small (~0.5 mL) volume of concentrated (27 %) HCl was added to the samples. Samples were centrifuged, decanted-rinsed until pH neutral and the supernatant came clean. Samples were rinsed into 99 % Glacial Acetic Acid, centrifugated-decanted, and then were treated using the Acetolysis reaction series. Acetolysis is triggered by the addition of a 9:1 solution of Acetic Anhydride and Sulfuric Acid, each at stock concentrations (99.5 % and 48 %, respectively). Samples were left in a 90 °C hot bath for 6 min, centrifuged, decanted, and rinsed in Glacial Acetic Acid, and then

Table 1
References and details on the four calibrations tested in this study. Comparison of temperature reconstructions based on these four calibrations are discussed in section S. 1.4.

Reference	Type	Calibration based on	n - r^2 - RMSE
Naafs et al. (2017)	Peat	Linear regression: $MAAT_{peat}$ = 52.18xMBT'_{5me} - 23.05	96–0.76–4.7 °C
Dearing Crampton-Flood et al. (2020)	Peat & Soil	Bayesian model based on MBT'_{5me}	343–0.70–3.8 °C ($BayMBT_0$)
Martínez-Sosa et al. (2021)	Lake	Bayesian model based on MBT'_{5me} (MAF)	272–0.82–2.9 °C
Véquaud et al. (2022)	Peat & Soil	Machine Learning (random Forest Regression)	661–0.83–2.5 °C ($FROG_0$)

centrifuged, decanted, and rinsed until pH neutral. Microbotanical fossils were recovered from the remaining residue using density separation in a solution of 5 % HCl and Zinc Bromide at a specific gravity of 2.3 g/mL. The material retrieved from the density separation was transferred into glycerine and stored in glass vials. Sample residues prepared in the laboratory were mounted on microscope slides and analyzed using a binocular microscope at 400x and 1000× magnification. Each slide was surveyed in linear transects, and all fossil pollen and *Lycopodium* sp. spores encountered were counted.

2.4.2. Pollen ecological assignment

2.4.2.1. Non-arboreal pollen and spores. Fern spores, aquatic plants, shoreline herbs, and grasses/sedges in the samples likely originate from the vegetation cover immediately local to the coring location. These types fall into some broad groups with consistent habitat preferences regarding inundation. Open-water pollen types including *Nymphaea* and *Nymphoides* are fully aquatic plants which prefer slow-moving open water, while wet shoreline communities include many Alismataceae (*Burnatia*-type pollen, also *Limnophyton*) and Haloragaceae, more infrequently *Lasimorpha senegalensis* and *Xyris*.

Both sedges (Cyperaceae) and grasses (Poaceae) are common in wetlands, but are also present in fully terrestrial conditions. These pollen types generally cannot be identified beyond the family level, which makes distinguishing wetland-specific genera or species impossible. Because sedges are predominantly affiliated with wetlands, they are classified with the local wetland vegetation. Poaceae pollen is included in the pollen sum as well as calculations of terrestrial pollen percentages.

Palms, which occur in swamp forests and wetland-affiliated plant communities, include *Eleis guineensis*, *Phoenix*, and *Raphia* (Table S. 2). These palms are also found in terrestrial settings, including under cultivation. *Pandanus* is a clearer indicator of riparian and wetland settings.

2.4.2.2. Arboreal pollen. Arboreal pollen types represent both the regional vegetation cover (*Daniella*-type, *Celtis*, etc.) as well as the composition of the flooded lowlands hydrologically linked to Ngaoundaba (*Syzygium*). There is substantial overlap in pollen types across these zones, both because of pollen taxa that occur across many vegetation communities (*Plantago*) and because of pollen taxa that lack sufficient morphological specificity (*Nauclea*-type, Urticaceae, Combretaceae-Melastomataceae). There are also pollen taxa that are taxonomically specific and have limited ecological tolerances (*Treculia africana*) that provide positive indicators of the presence of these conditions in the Ngaoundaba area. Many of the most common pollen taxa have affiliations with forested wetlands, riparian zones, and lakesides (*Alchornea*, *Macaranga*, *Mallotus oppositifolius*, and *Syzygium*). All pollen taxa, growth forms, and ecological assignments are listed in Table S 2.

2.5. Statistical treatment

Statistical treatment was performed using R software. We performed constrained hierarchical clustering using the "chclust" function from the "rioja" package, that constrained samples based on their (chronological) order (Juggins and Juggins, 2019). Therefore, unlike unconstrained clustering, the clusters can only be merged if they are stratigraphically adjacent. The matrix of dissimilarity was created using the "vegdist" function from the "vegan" package (Oksanen et al., 2013) with Bray-Curtis distance, and the agglomeration method was the Coniss method.

3. Results

3.1. Organic geochemistry data

3.1.1. n-Alkanes

3.1.1.1. Abundance and concentration. The most abundant *n*-alkanes are *n*-C_{29}, *n*-C_{31} and *n*-C_{33} alkanes, except for a few samples around 8.5-8.2 ka cal BP which are dominated by *n*-C_{23} alkane. The *n*-C_{31} alkane represents between 11 and 30 % of the *n*-alkane assemblages with a mean value of 19 % (Fig. 1). Low relative abundances are recorded before 3.5 ka cal BP with values generally below 20 %. Minimum values occur around 8.2 ka cal BP and around 4 ka cal BP while maximum values occur around 3 ka cal BP. During the late Holocene, *n*-C_{31} relative abundance presents intermediate values between 18 and 25 %. The *n*-C_{31} alkane concentration ranges between 8 and 57 $\mu g/g_{TOC}$ with a mean value of 25 $\mu g/g_{TOC}$ (Fig. 2). The *n*-C_{29} alkane represents between 8.7 and 56.7 % of the *n*-alkane assemblages, with a mean value of 16.9 %. The *n*-C_{29} alkane concentration ranges between 5 and 214 $\mu g/g_{TOC}$ with a mean value of 24 $\mu g/g_{TOC}$. Peaks in n-C_{29} concentration and relative abundance are recorded at 8.8-8.5 and 8.1 ka cal BP and between 4.5 and 3.5 ka cal BP. The *n*-C_{33} alkane represents between 3.6 and 25.0 % of the *n*-alkane assemblages, with a mean value of 15.1 %. The *n*-C_{33} alkane concentration ranges between 4 and 51 $\mu g/g_{TOC}$ with a mean value of 20 $\mu g/g_{TOC}$, its variations following those of the *n*-C_{31} concentration.

3.1.1.2. n-Alkane ratios: CPI, ACL, P_{aq}. CPI values range from 4 to 45 with an average value of 11 (Fig. 2), in the range of the CPI values of fresh plant material (4–40 in plants with different photosynthetic metabolism types (C_3, C_4, CAM) (Collister et al., 1994), and 2 to 50 for equatorial east African plants (Griepentrog et al., 2019)). There is no clear correlation with depth. The topmost sample presents a higher CPI, likely resulting from less degraded plant material (Lehtonen and Ketola, 1993; Killops and Killops, 2013). Two periods of increase in CPI values can be noted, at 8.7 ka cal BP and from 3.5 to 2.8 ka cal BP possibly resulting from changes in *n*-alkane sources. The CPI increase around 8.7 ka cal BP is due to the very high concentration of *n*-C_{29}, leading to difficulties in integrating small peaks in GC analyses, i.e., peaks of even-numbered *n*-alkanes.

The $ACL_{27\text{-}33}$ ranges from 29.1 to 31.1 with a mean value of 30.4 (Fig. 2). Two periods of lower ACL values can be noted around 8.7 ka cal BP and from 4.5 to 3.5 ka cal BP. In addition, the topmost sample also presents a lower ACL value.

P_{aq} values range from 0.1 to 0.6 with an average value of 0.4 (Fig. 2). A sharp decrease in P_{aq} values driven by a brief increase in the abundance of *n*-C_{29} followed by a sharp increase in P_{aq} is recorded between 8.9 and 8.2 ka cal BP (Fig. 2).

3.1.1.3. Carbon isotopic composition of long-chain n-alkanes. The $\delta^{13}C_{n\text{-}C31}$ values range from −32.0 to −22.9 ‰ with a mean value of −28.3 ‰ (Fig. 3). During the early Holocene from 9.7 to 9.4 ka cal BP, $\delta^{13}C_{n\text{-}C31}$ values range between −24.6 and −23.9 ‰. The $\delta^{13}C_{n\text{-}C31}$ values then rapidly get more ^{13}C-depleted and present short-term variations up to around 8.0 ka cal BP. Stable values around −30 ‰ are recorded from 8.0 to 5.5 ka cal BP. After 5.5 ka cal BP, the $\delta^{13}C_{n\text{-}C31}$ values are above −30 ‰ with short negative incursions around 4.6, 0.8 and after 0.5 ka cal BP. The $\delta^{13}C_{n\text{-}C29}$ values are more ^{13}C-depleted than the $\delta^{13}C_{n\text{-}C31}$ values, ranging from −33.7 to −25.6 ‰ with a mean value of −30.8 ‰. The $\delta^{13}C_{n\text{-}C29}$ values present similar variations as the $\delta^{13}C_{n\text{-}C31}$ values except between 8.9 and 7.9 ka cal BP where the $\delta^{13}C_{n\text{-}C29}$ values present only a slight increase. The $\delta^{13}C_{n\text{-}C29}$ values get heavier during the last 1.0 ka cal BP. The $\delta^{13}C_{n\text{-}C33}$ values range from −32.3 to −23.4 ‰ with a mean value of −28.1 ‰ and its variations closely follow those of $\delta^{13}C_{n\text{-}C31}$ values.

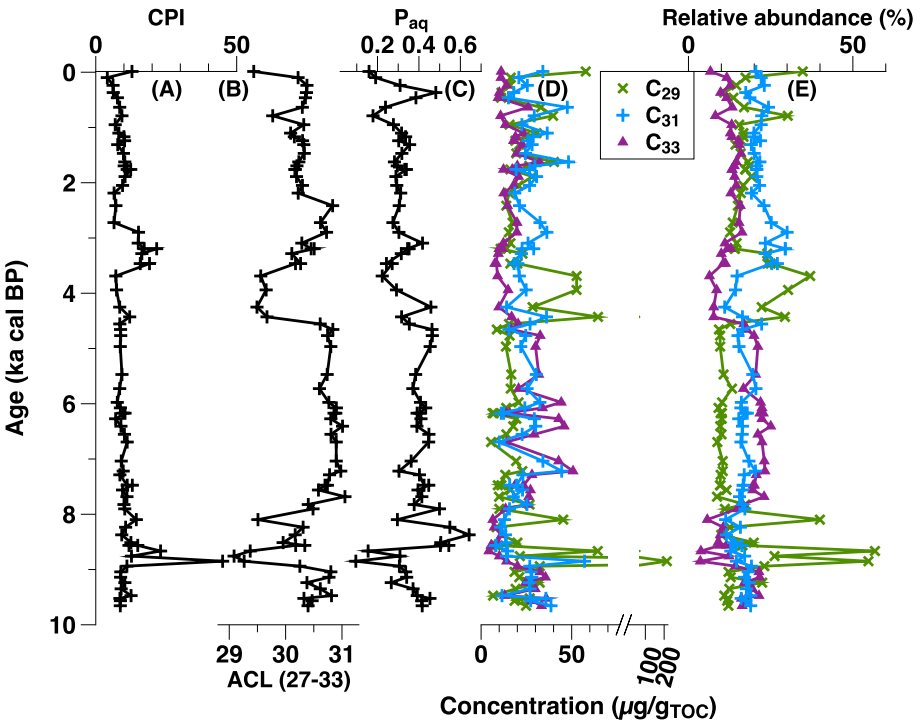

Fig. 2. n-Alkane data from the Ngaoundaba peat deposit. (A) Carbon Preference Index -CPI-, (B) Average Chain Length -ACL- (based on n-C27 to n-C33 alkanes), (C) P_{aq} ratio, (D) Concentration of *n*-C_{29}, *n*-C_{31} and *n*-C_{33} alkanes in $\mu g/g_{TOC}$. (E) Relative abundances of *n*-C_{29}, *n*-C_{31} and *n*-C_{33} alkanes (taking into account *n*-alkanes from *n*-C_{19} to *n*-C_{37}). Ratios were presented in section 2.3.2.2.

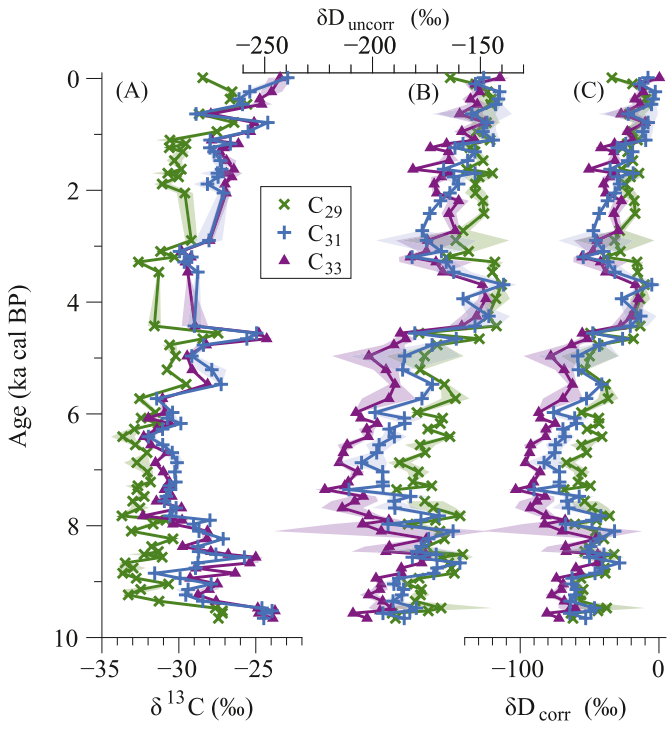

Fig. 3. Carbon and hydrogen isotopic composition of *n*-C_{29}, *n*-C_{31} and *n*-C_{33} alkanes. δD_{corr} values were corrected for vegetation changes using $\delta^{13}C_{n\text{-}alk}$ values as presented in section 2.3.2.4.

3.1.1.4. Hydrogen isotopic composition of long-chain n-alkanes. The $\delta D_{n\text{-}C31}$ values (corrected for vegetation changes) range from −90 to −3 ‰ with a mean value of −44 ‰ (Fig. 3). The early Holocene is characterized by intermediate values around −50/−60 ‰ until 8.8 ka cal BP. Most D-depleted values are recorded between 7.4 and 5.8 ka cal BP. The $\delta D_{n\text{-}C31}$ values increase towards the end of the Holocene. Two 1-ka periods of less D-depleted values centered at 8.2 and 4 ka cal BP can be noted. $\delta D_{n\text{-}C29}$ and $\delta D_{n\text{-}C33}$ present similar variations as the $\delta D_{n\text{-}C31}$ with $\delta D_{n\text{-}C29}$ being slightly D-enriched and $\delta D_{n\text{-}C33}$ being slightly D-depleted compared to the $\delta D_{n\text{-}C31}$. After around 8.2 ka cal BP, the $\delta D_{n\text{-}C31}$ and $\delta D_{n\text{-}C33}$ return to more D-depleted values, while the $\delta D_{n\text{-}C29}$ values remain more D-enriched. The period of D-enrichment around 4 ka cal BP starts around the same time for all three *n*-alkanes but its conclusion differs with $\delta D_{n\text{-}C31}$ and $\delta D_{n\text{-}C33}$ ending around 3.5 ka cal BP, while $\delta D_{n\text{-}C29}$ concludes around 3.2 ka cal BP.

3.1.2. GDGTs and brGDGT-based temperature reconstruction

3.1.2.1. Relative abundances, concentrations and MBT'$_{5Me}$ ratio. The GDGT assemblages are predominantly composed of brGDGTs, representing between 67 and 92 % of the overall GDGT assemblages. The predominant brGDGT is brGDGT-Ia, which represents 52–78 % of the brGDGT assemblages. The concentration of brGDGT-Ia ranges from 45 to 194 $\mu g/g_{TOC}$ with an average value of 96 $\mu g/g_{TOC}$. The concentration of brGDGT-Ia is elevated prior to 5.8 ka cal BP, exceeding 100 $\mu g/g_{TOC}$, with the exception of a brief interval of decreasing values between about 9 and 8 ka cal BP. Following 5.8 cal BP, the concentration of brGDGT-Ia diminishes, with all measurements but one falling below 100 $\mu g/g_{TOC}$. The relative abundance and concentration of brGDGTs decrease with an increasing number of methylations (Ia to IIIa) and a high degree of cyclisation (Ia to Ic).

IsoGDGT-0 is the predominant isoGDGT, constituting 74–93 % of the isoGDGT assemblages. IsoGDGT-0 concentrations vary from 6 to 24 $\mu g/g_{TOC}$. The MBT'$_{5Me}$ ratio ranges between 0.7 and 0.9 (Fig. 4 A). Prior to 5.8 ka cal BP, the MBT'$_{5Me}$ exhibits the peak values in the record, with a singular decrease occurring at 8.7 ka cal BP. Following 5.8 ka cal BP, two intervals of elevated MBT'$_{5Me}$ values are documented about 4 ka cal BP and subsequent to 0.5 ka cal BP.

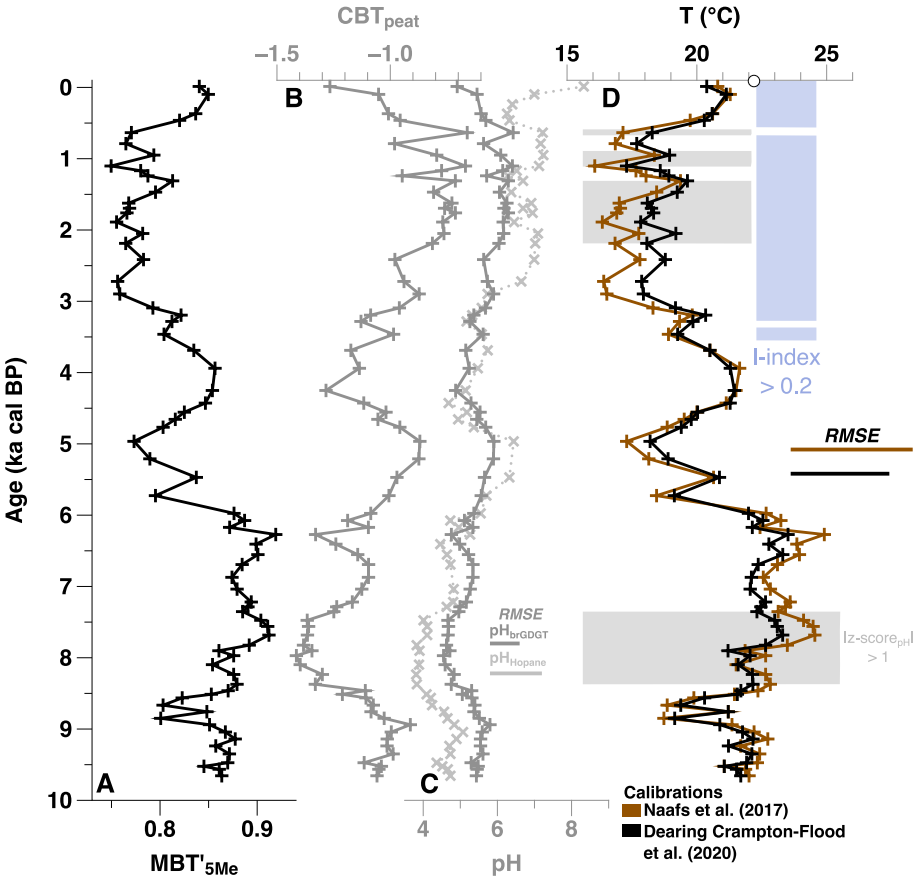

Fig. 4. brGDGT records from the Ngaoundaba peat deposit. (A) MBT'$_{5Me}$ ratio, (B) CBT$_{peat}$, (C) brGDGT- and hopane-reconstructed pH (Schaaff et al., 2024), (D) brGDGT-based temperature reconstructions. The present-day MAAT at the Ngaoundaba peat deposit is indicated by a white circle. On panel (D), the light grey range highlights z-score values based on pH above 1 or under −1 (Schaaff et al., 2024) and the light blue range highlights I-index values above 0.2 (Schaaff et al., 2023). (For interpretation of the references to color in this figure legend, the reader is referred to the Web version of this article.)

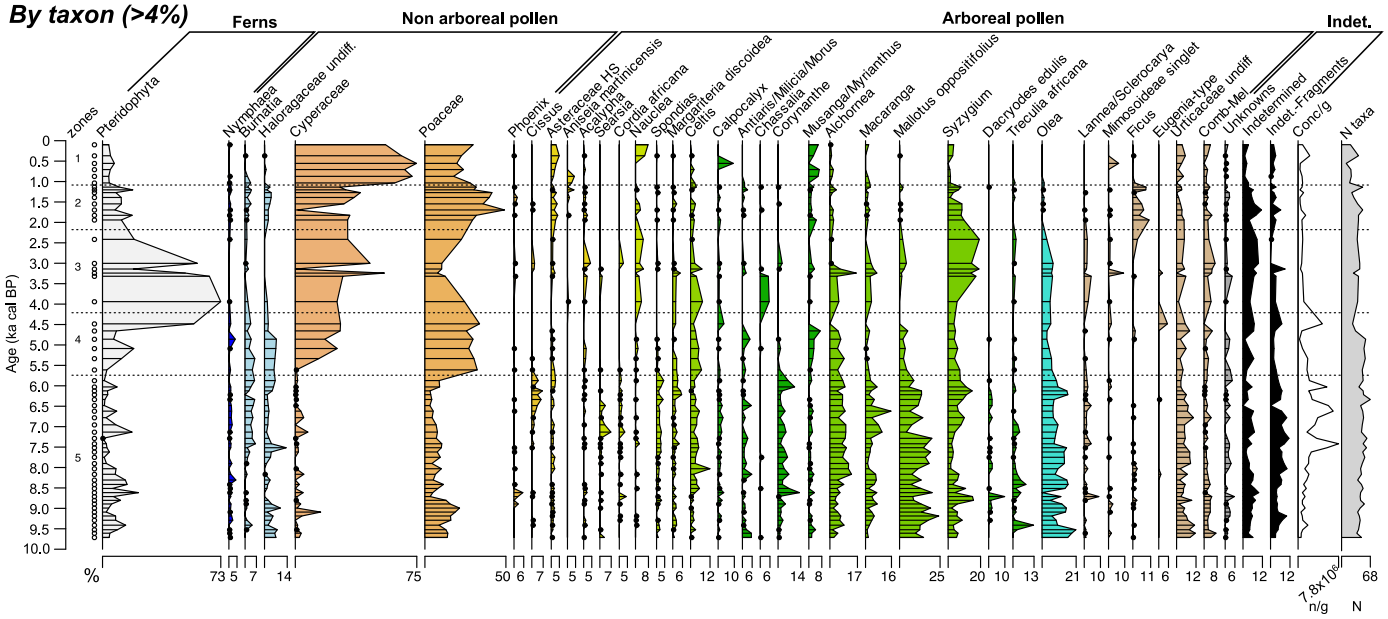

Fig. 5. Pollen diagram in the Ngaoundaba peat (in %). Pteridophyta are calculated as percent of total palynomorphs identified. Non-arboreal pollen plants are calculated as percent of total palynomorphs identified, excluding Pteridophyta. Arboreal pollen types are calculated separately, taking into account arboreal pollen and Poaceae. The color coding is based on ecological affiliation of each taxon. Concentration is expressed as the number of pollen grains per gram of sediment. Some taxa/pollen types were identified but constitute less that <4 % and are consequently not shown in this figure, these taxa are presented in Table S.2. Indet.: indeterminable, N taxa: Number of taxa. (For interpretation of the references to color in this figure legend, the reader is referred to the Web version of this article.)

3.1.2.2. Temperature reconstructions. brGDGT-based temperature values based on the temperature calibration from Naafs et al. (2017) range from 16.1 to 24.9 °C with a mean value of 20.5 °C, temperature values based on the $BayMBT_0$ calibration (Dearing Crampton-Flood et al., 2020) range from 17.3 to 23.5 °C with a mean value of 20.6 °C (Fig. 4 D).

For the $BayMBT_0$ calibration, the temperature range is 6.2 °C for the Holocene. This range of temperature is above the calibration error of the $BayMBT_0$ calibration. From 10 to around 5.8 ka cal BP, brGDGT-reconstructed temperature values are above 20 °C except a brief decrease to around 19 °C between 8.9 and 8.5 ka cal BP. After 5.7 ka cal BP, lower temperature values around 18–19 °C are recorded: this period is interrupted by a 1-ka-long increase in temperature centered around 4 ka cal BP. A marked increase of around 2 °C is recorded during the late Holocene after 0.5 ka cal BP. The temperature record based on the calibration Naafs et al. (2017) has slightly amplified temperature variations.

3.2. Pollen data

All pollen taxa, growth forms, and ecological assignments are listed in Table S. 2. Fig. 5 presents pollen diagrams by taxa of the Ngaoundaba peat, while Fig. 6 shows pollen results grouped by ecological zones. Five pollen zones were defined based on major variations in the pollen spectra (Fig. 7) and are represented in Figs. 5 and 6. Figure S. 6 presents a summary of fern, arboreal, and non-arboreal percents. Pollen percentages were calculated without taking into account fern spores. Details on percentage calculation are given in the caption of each figure.

3.2.1. General pollen data

Patterns in the overall pollen concentration (Fig. 5) indicate an initial phase characterized by typically reduced pollen concentrations for both arboreal and non-arboreal pollen types from 9.7 to 7.7 ka cal BP (between 0.6 and 2.1 $\times$ 10^6 per gram). A significant increase in pollen concentrations, especially among arboreal pollen types, follows between 7.6 and 5.9 ka cal BP. In this phase, tree/shrub pollen typically constitutes over 70 % of the total pollen concentration. This phase has three peaks ranging from 5.7 to 7.2 $\times$ 10^6 per gram at approximately 7.4, 6.6, and 6.0 ka cal BP, with values declining to background levels of 1.2-3.9 $\times$ 10^6 per gram in between. The average background level remains elevated compared to amounts recorded after 7.7 ka cal BP and prior to 3.1 ka cal BP. Total concentrations decline from 6.0 to 5.3 ka cal BP, reaching a low of 0.2 $\times$ 10^6 per gram. With the exception of a sharp peak about 4.5 ka cal BP, reaching a core-wide high of 4.7 $\times$ 10^6 per gram, pollen concentrations beyond this period are very low, ranging from 2.2 to 0.2 $\times$ 10^6 per gram.

The number of pollen types throughout the core remains rather consistent, peaking at 68 identified pollen types around 6.3 ka cal BP and declining to a minimum of 10 taxa at 0.5 ka cal BP (Fig. 5). The quantity of identified pollen types exhibits a slight increase from the base of the core to 5.1 ka cal BP. Richness declines from around 50 taxa to about 30 taxa after 4.9 ka cal BP, but rebounds slightly between 3.3 and 1.5 ka cal BP, reaching approximately 40 taxa. The number of pollen taxa seen generally decreases after approximately 1.3 ka cal BP, with exceptions at peaks around 1.2-1.1 and 0.3 ka cal BP.

The overall composition of pollen and spores analyzed from Ngaoundaba shows a broad dominance of arboreal pollen types between 9.7 and 5.9 ka cal BP, representing more than 55 % of the pollen assemblages (Figs. 5 and 6 and S.6). There are slight and inversely related fluctuations in the proportions of herbs/forbs and ferns (Fig. 6). Ferns (Pteridophyta) are abundant, representing around 15 % of total palynomorphs, and herbs/forbs are less common at around 9.5 and 8.6 ka cal BP (Fig. 6). After 5.9 ka cal BP, there is a turnover as herbs/forbs become the most abundant pollen types by around 5.1 ka cal BP and are subsequently swamped by a sudden pulse of enhanced fern spore influx from 4.7 to 3.0 ka cal BP reaching an abundance of >70 % (Figs. 5 and 6). Arboreal pollen types experience a modest and staggered increase between 2.4 and 1.1 ka cal BP, but herbs/forbs show a steep rebound from 3.1 to 1.0 ka cal BP, after which there is a minor shift in favor of trees/shrubs up to 0.1 ka cal BP (Figure S6).

3.2.2. Local wetland pollen signal

Between approximately 9.7 and 8.0 ka cal BP, the herbaceous wetland assemblage exhibits a more balanced distribution between species favoring complete inundation (*Nymphaea*) and those that inhabit both wetland and terrestrial environments (Cyperaceae and Poaceae) (Fig. 5). Between 8.3 and 7.7 ka cal BP, inundated and shoreline types decreased in prevalence, with values falling below 2 and 5.2 %, respectively. However, from 7.5 to 4.9 ka cal BP, these types become more common, with shoreline types approaching 15 % around 7.5 and 5.8 ka cal BP (Fig. 6). Fern spores exhibit an anti-phase relationship with inundated/shoreline types, displaying minor peaks at 9.4 (22 %) and 8.5

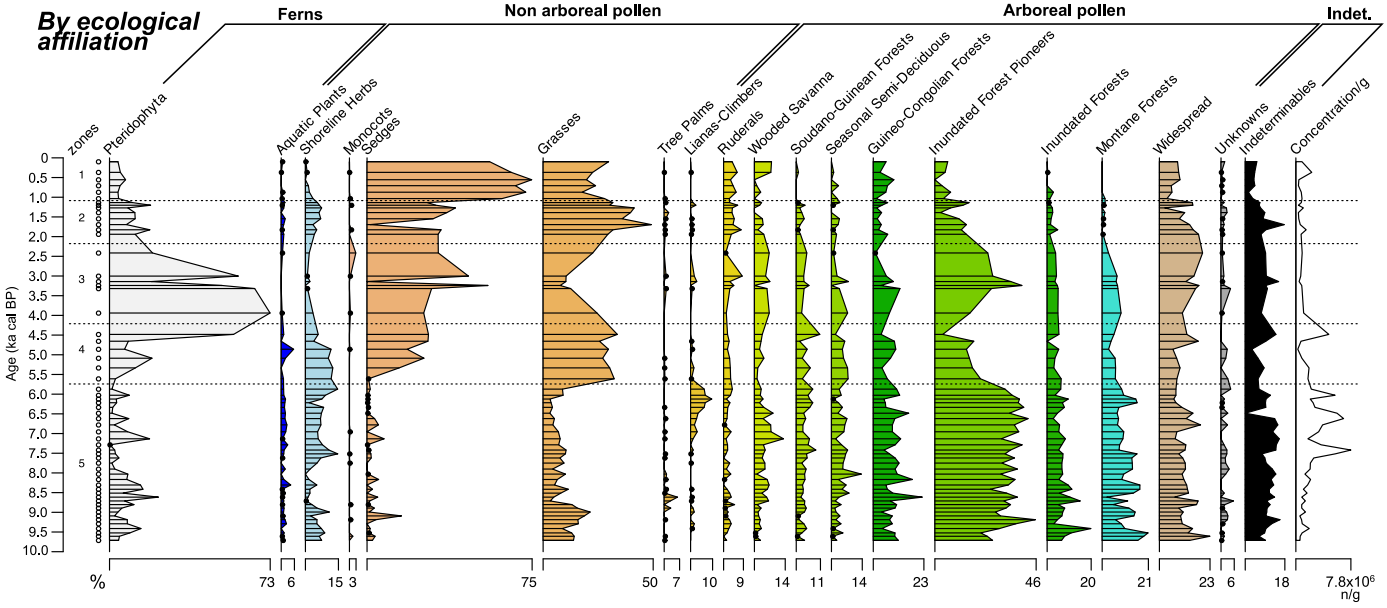

Fig. 6. Pollen results presented as percents and grouped by ecological zones. The ecological assignment of each taxon is given in table S. 2.

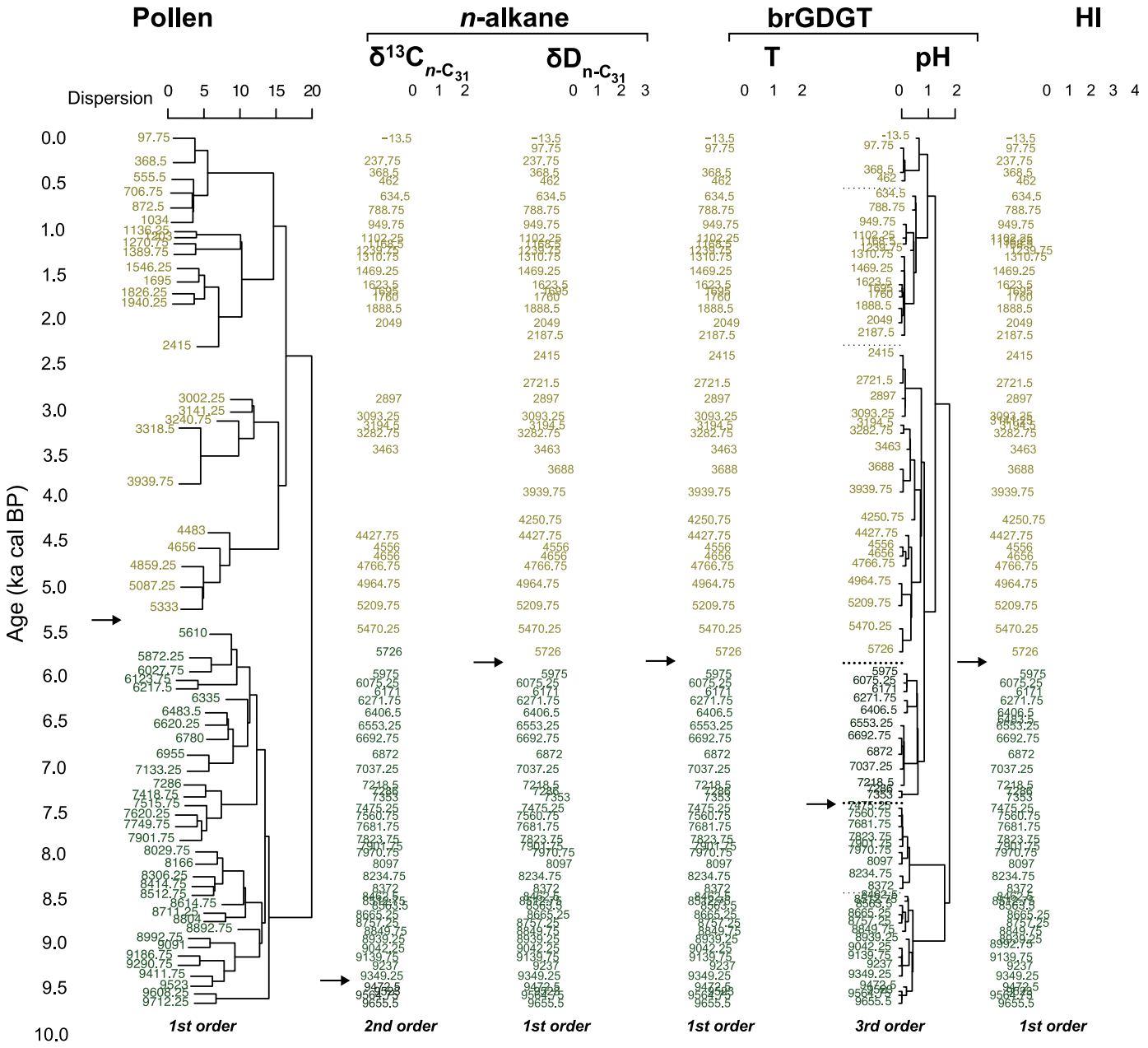

Fig. 7. Cluster analyses of main organic biomarker and pollen data from the Ngaoundaba peat record. In each panel, the black arrow highlights the first-order zonation.

(15 %) ka cal BP, subsequently approaching minimum values at 7.3 ka cal BP (Fig. 6 and S6). Trees palms (including *Pandanus*) reach their maximum influx around 8.7-8.6 ka cal BP, constituting up to 6 % of arboreal and grass pollen (Fig. 6). From 7.7 to 4.7 ka cal BP, the local herbaceous signal is dominated by open water and shoreline types, exhibiting notably higher abundances between 7.3 and 6.2 ka cal BP (Fig. 6). Ferns, sedges, and grasses are at some of their lowest abundances through this section of the core (Fig. 6), with *Raphia* being the only palm consistently present (data not shown, see table S.2 – included in tree palms on Fig. 6).

This trend shifts between 6.2 and 2.4 ka cal BP, characterized by a decline in open water and shoreline communities, while families such as sedges and grasses reach some of their highest values in the record (Figs. 5 and 6). This occurs in a sequential manner, with grasses initially increasing between approximately 5.5 and 3.9 ka cal BP, while sedges rise during this phase to a local maximum at 3.2 ka cal BP. From 4.5 to 3.2 ka cal BP, the proportion of fern spores among identified palynomorphs increases significantly, peaking at over 70 % around 3.9 ka cal BP and subsequently reaching 60 % at 3.0 ka cal BP (Figs. 5 and 6). This phase is characterized by the minimal representation of open water and wet shoreline types, with nearly no recovery of open water types between 3.3 and 3.0 ka cal BP (Fig. 6). *Phoenix* occurs in small numbers within these samples, whereas *Raphia* or *Pandanus* were not recovered in this section (data no shown but included in tree palms in Fig. 6).

From 2.4 to 1.1 ka cal BP, a low-amplitude increase in open water and shoreline types is observed relative to other wetland types, while the overall influx of grasses and sedges concurrently rises throughout this section of the core (Fig. 6). Fern representation drops during this period, while *Phoenix* and *Pandanus* are present in limited amounts. The latter predominantly disappears from the Ngaoundaba record above this section. Post 1.1 ka cal BP, open water and shoreline types constitute approximately 1 % of the total pollen influx (Fig. 6). Grasses were prevalent at 1.1 ka cal BP, while sedges became similarly prominent in this uppermost section, comprising 55–75 % of the pollen assemblage,

displacing other wetland types and ferns (Fig. 6).

3.2.3. Regional arboreal pollen signal

Arboreal pollen types are prominently represented between 9.7 and 5.6 ka cal BP, driving the general trend of increasing concentration values from the base of the core to 5.6 ka cal BP (Fig. 6 and S6). *Olea* serves as the primary representative of regional montane plant communities, presenting a notable prevalence in the lowermost samples, comprising 21 % of arboreal & grasses pollen. Its representation is significant throughout a substantial portion of the Ngaoundaba record, ranging from 10 to 18 % (Fig. 5). Pollen from the Urticaceae family follows a consistent pattern, reaching a peak of 18 % in the lowermost samples and maintaining approximately 10 % until 5.6 ka cal BP (Fig. 5). Plants within the Urticaceae family belong to diverse ecosystems and are categorized into different pollen types; however, in the context of Ngaoundaba, it is plausible that these originate from the common rainforest herb *Laportea*. Pollen indicative of various vegetation types, such as wooded savanna (*Daniellia*, *Lannea/Sclerocarya*), seasonal semi-deciduous forests (*Celtis*, *Trema orientalis*), inundated forest pioneers (*Alchornea*, *Macaranga*, *Mallotus oppositifolius*), and Guineo-Congolian rainforests (*Corynanthe*, Sapotaceae, *Pseudospondias*), occurs at lower frequencies in the lowermost samples compared to those above (Fig. 5). At 9.2 ka cal BP, the Ngaoundaba record is predominantly characterized by pollen from various Guineo-Congolian forest associations, particularly *Mallotus oppositifolius* and *Syzygium* (Fig. 5). The lower section of the core (9.2-5.6 ka cal BP) is dominated by arboreal types associated with seasonal and evergreen forest environments (Fig. 6). It contains a balance of heliophiles/pioneers, seasonal semi-deciduous forest types, and taxa typical of closed forest settings in regularly inundated geomorphological contexts (*Mallotus oppositifolius*, *Treculia africana*).

This forest-dominated section of the core exhibits minor fluctuations in the abundance of various arboreal pollen types. *Cordia africana*, *Treculia africana*, *Searsia*, *Dacryodes edulis*, and *Corynanthe*-type pollen represent significant components of the forest signal between 9.2 and 6.1 ka cal BP (Fig. 5). However, they are among the initial forest-associated pollen types to either decline or vanish before the substantial shift in arboreal and non-arboreal pollen observed at 5.6 ka cal BP. During this period, *Macaranga*-type and *Alchornea* pollen progressively replace *Mallotus oppositifolius*, accompanied by a notable rise in lianas and climbers, including *Cissus* and *Allophylus,* between 7.2 and 5.6 ka cal BP (Fig. 5). *Syzygium* exhibits increased abundance in samples dating to approximately 5.6 ka cal BP and is among the limited arboreal types that show a rise in abundance post 5.6 ka cal BP (Fig. 5). Several pollen taxa are consistently present throughout this time span, although at relatively low frequencies, and continue to persist in the upper sections of the core where non-arboreal pollen are more prevalent. The taxa include *Celtis*, *Lannea/Sclerocarya*, Combretaceae-Melastomataceae, *Croton*-type, *Antiaris/Milicia/Morus*, and *Margariteria discoidea* (Fig. 5).

Between 5.6 and 1.9 ka cal BP, there is a consistent decline in montane taxa culminating in their near disappearance from the pollen assemblage. *Searsia* is completely absent from the record following this point, while *Olea* is present at low frequencies, approximately 1 %, in a limited number of subsequent samples (Fig. 5). Certain arboreal pollen types show a slight increase in abundance during this phase, especially those with distributions that extend across the transitional zones north of the Guineo-Congolian forest zone, including *Nauclea*-type, *Musanga/Myrianthus*, *Celtis*, *Syzygium*, and *Lannea/Sclerocarya* (Fig. 5). The influx of all arboreal pollen types gradually decreases from 5.6 to 1.9 ka cal BP. From this point until approximately 1.1 ka cal BP, the arboreal pollen assemblage exhibits less diversity and constitutes a smaller proportion of the total assemblage. Taxa exhibiting pan-tropical distributions typically constitute minor components of the pollen assemblage in the majority of the cases. *Ficus* represents an exception to this trend, exhibiting its highest prevalence during this period, while *Syzygium* ranks as the second most prevalent arboreal pollen type (Fig. 5). The significant reduction in the arboreal component of the pollen assemblage persists from 1.1 to 0.1 ka cal BP, during which only the most widely distributed taxa (*Celtis*, *Nauclea*-type, *Myrianthus/Musanga*) are observed at markedly lower percentages relative to the earlier phase of the record (Fig. 5).

3.3. Cluster analyses

At the Ngaoundaba peat deposit, cluster analyses derived from the hydrogen isotopic composition of *n*-C_{31} alkane, GDGT-based temperature reconstruction, hydrogen index (HI) (Schaaff et al., 2023) and pollen reveal a first-order division occurring approximately between 5.5 and 5.8 ka cal BP (Fig. 7). Likewise, for GDGT-based pH reconstruction and carbon isotopic composition of *n*-alkanes, a second or third order division occurs within the same timeframe (Fig. 7).

4. Discussion

4.1. Vegetation dynamics during Holocene

4.1.1. Local wetland vegetation dynamics

The abundance of local wetland plants tracks hydrological conditions at Ngaoundaba. Among the pollen types belonging to the local wetland context, inundated and shoreline plants dominate wetland vegetation prior to 5 ka cal BP. These plants are prevalent between 9.6 and 8 ka cal BP, but are inconsistent and exhibit significant variability between samples. By 8 ka, they are consistently abundant and peaking between 7.3 and 6.2 ka cal BP. This indicates permanent standing water at a level too high to allow the development of Cyperaceae on the peat surface (Fig. 8). Between 6 and 5 ka cal BP, there is a significant rise of the proportion of Cyperaceae pollen, indicating the spread of Cyperaceae and grasses on the wetland surface as the water level falls (Fig. 8). Fern spores exhibit a sudden peak between 4.5 and 3 ka cal BP, potentially indicating increased terrestrialization of the site. The aquatic pollen signal aligns with the P_{aq} ratio at Ngaoundaba (Fig. 8), indicating rapid alterations in aquatic vegetation between 9 and 8 ka cal BP and a significant decrease about 4 ka cal BP. Brief intervals of wetland expansion are seen at around 2-1.5 ka cal BP and 4-3.5 ka cal BP. The combined local pollen signal and P_{aq} indicate stable water conditions until approximately 6 ka cal BP, succeeded by rapid terrestrialization of the site between 5 and 3 ka cal BP, which, aside from a slight increase in open water between 2.5 and 1 ka cal BP, persists until the present day.

The graduate transition in $\delta^{13}C_{n\text{-alk}}$ records towards more ^{13}C-enriched values after 6-5 ka cal BP indicates a shift towards a C4-dominated ecosystem, reflecting the substantial contributions of *n*-alkanes from sedges and grasses to the peat. Prior to 6-5 ka cal BP, the transition towards more ^{13}C-enriched $\delta^{13}C_{n\text{-}C31}$ values at approximately 9-8 ka cal BP corresponds with a phase of significant changes in wetland vegetation (Fig. 8). Consequently, the carbon isotopic composition of *n*-alkanes indicates a local signal, predominantly derived from local vegetation. Long-chain *n*-alkanes are mainly synthetized by higher plants, with *n*-C_{33} and *n*-C_{31} often more prevalent in grasses, whilst *n*-C_{29} is more abundant in trees and shrubs (e.g., Vogts et al., 2009), explaining the variations observed in $\delta^{13}C_{n\text{-alk}}$ records (Fig. 10). At Ngaoundaba, the simultaneous rise in fern spores and *n*-C_{29} alkane concentration between 4.5 and 3.5 ka cal BP indicates that ferns may have been a significant source of *n*-C_{29} alkane during this timeframe, corroborating existing research (Lytle et al., 1976).

4.1.2. Regional vegetation dynamics

Apart from the major changes in local wetland dynamics, the pollen analyses from the Ngaoundaba deposit highlight the regional changes in vegetation occurring on the eastern Adamawa plateau during the last 10 ka cal BP. From the beginning of the Holocene to around 5.6 ka cal BP, a forested environment dominates the region and presents a complex diversity, including taxa from wooded savannas, Sudano-Guinean forests, seasonal semi-deciduous forests, Guineo-Congolian forests, and montane forests, while grasses never represent more than 21 % of the

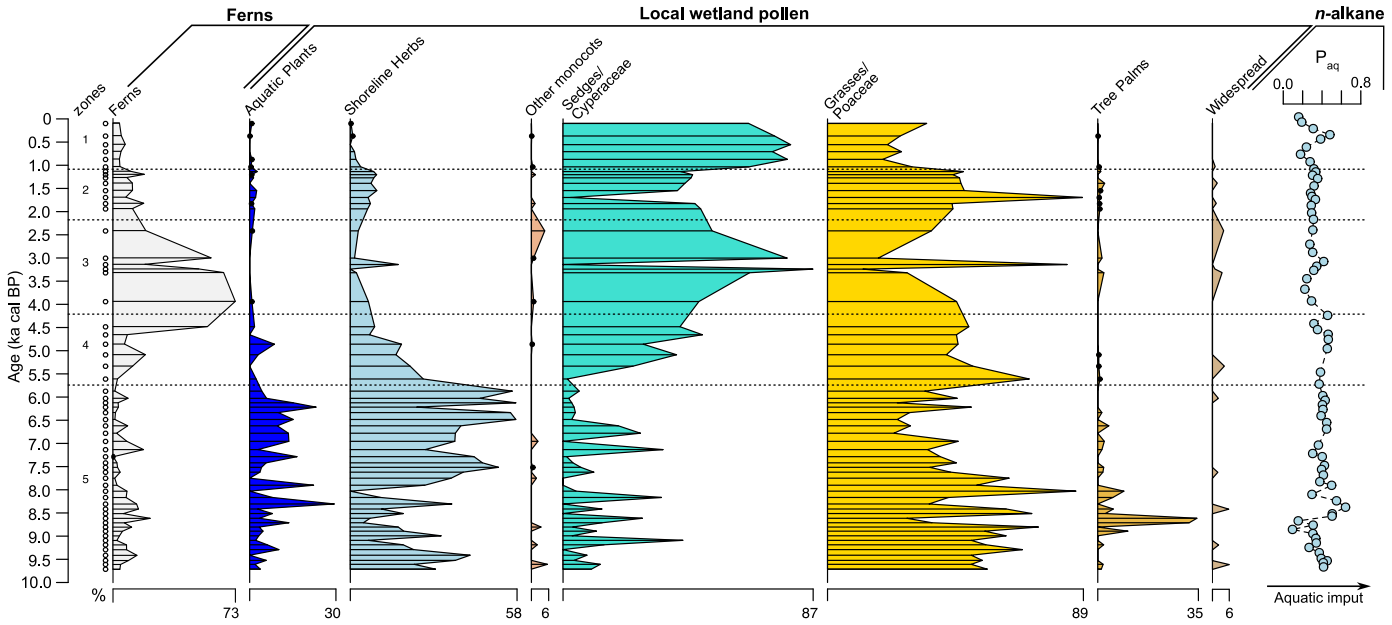

Fig. 8. Proportion of wetland vegetation and Paq ratio. Ecological affiliation for pollen taxa are presented in Table S. 2. Local wetland pollen groups are calculated as percent of total local wetland pollen. Ferns are calculated as percent of total palynomorphs identified. Paq ratio is presented in section 2.3.2.2.

terrestrial pollen assemblage (Fig. 6). The region was thus consistently forested between 10 and 5.6 ka cal BP. The Ngaoundaba peat records the northward migration of vegetation zone boundaries, consistent with observations made in neighboring Lake Mbalang and Lake Tilla in northeastern Nigeria (Salzmann et al., 2002; Vincens et al., 2010).

In line with the chronology observed in the pollen record from lake Mbalang (Vincens et al., 2010), forest decline is recorded from around 6.1 ka, with the disappearance of several taxa characteristic of Guineo-Congolian and inundated forests, particularly pioneers. Taxa indicating closed forests with high water tables such as *Mallotus oppositifolius* and *Treculia africana* are replaced by others such as *Macaranga* and *Alchornea*. A major turnover occurs around 5.6 ka cal BP, where an arboreal-dominated pollen assemblage transitions to a herbaceous-dominated pollen assemblage within a few hundred years (Fig. 6, S6). The Ngaoundaba pollen record highlights the gradual decline of forested elements after 5.6 ka cal BP, losing both diversity and abundance, which is consistent with neighboring pollen records (Lebamba et al., 2016; Vincens et al., 2010). Some taxa with a larger climatic amplitude and affinities for open shorelines, such as *Syzygium* (Watrin et al., 2007) (Fig. 5), persist through the mid- and late Holocene, and even show some periods of increase.

Olea persists until around 2.2 ka cal BP and then falls to less than 2 % of the terrestrial pollen assemblage until 0.9 ka cal BP, when it completely disappears from the Ngaoundaba pollen record (Fig. 5). The long persistence of the montane forest taxa *Olea capensis* is a specific feature of the Adamawa plateau highlighted by Vincens et al. (2010) and associated with the altitudinal position of the sites.

The opening of the regional environment reflects changes in climatic settings mainly driven by changes in either the amount or seasonality of precipitation. The disappearance of seasonal semi-deciduous forest and montane taxa strongly argues for a change in the seasonality of precipitation with an increase in the duration of the dry season in addition to a decrease in precipitation amount (Vincens et al., 2010). *Daniella*-type pollen is recorded at low frequencies until 5.6 ka cal BP and persisting until 2.2 ka cal BP. This taxon has a limited temperature range (Watrin et al., 2007) and could indicate a decrease in temperature during the Holocene.

4.2. *Hydroclimatic record of the end of the AHP at Ngaoundaba based on n-alkanes*

4.2.1. *Influence of wetland vegetation on δD values of n-alkanes*

The Ngaoundaba peat deposit presents large variation in δD of *n*-alkanes for the considered period (87.4‰) (Figs. 3 and 10), compared to other records from tropical and subtropical Africa (Table S.1) such as Lake Barombi (34.8‰) or Lake Bosumtwi (31‰) over the same period. This apparent difference reflects the impact of local vegetation and its evolution through time on the δD record. The transition from open water to gradual terrestrialization of the peatland impacts the relative contribution of the main sources of *n*-C_{31} alkane (Fig. 9). In addition, due to the marked seasonality of precipitation, the water level in the peat varies considerably between the monsoon rainy season and the dry season. During the dry season, peat water can become enriched in deuterium through evaporation, which may lead to further enrichment of the δD_{wax} of plants using this water. Transpiration does not produce isotopic fractionation of peat water (e.g., Gibson and Edwards, 2002), but does affect the isotopic composition of leaf water (Sachse et al., 2012 and references therein). Peat water is defined as the water that accumulates in wetlands, while leaf water refers to the water contained within plant leaves, where *n*-alkanes are predominantly produced. During the late Holocene, this is likely to affect the δD_{wax} values of sedges and grasses, which during this period represent a significant input of *n*-C_{31} alkane. This effect led to a further enrichment of δD_{wax} values during a period of already D-enriched δD_{wax} values compared to the AHP therefore increasing the range of δD_{wax} values (Fig. 9). Such an enrichment in deuterium is recorded in closed basins, such as in a nearby lake on the Adamawa Plateau (Lake Tizong) (Abba et al., 2023). A strongly deviated regional meteoric water line, indicating a D-enrichment of the water in each basin relative to precipitation water, was also recorded in south-west Tanzania (Delalande et al., 2008).

Other tropical peatlands evidence similar isotopic enrichments. The 4-ka δD_{wax} record from the Kyambangunguru peat deposit (Coffinet et al., 2018) presents a large range of δD_{wax} values (36–76‰ depending on the chain length), which is far above the range of δD_{wax} values in other East African lakes. Similarly, the $\delta^{18}O_{cellulose}$ values from the Kashiru peatland (Burundi) present a range of around 9‰ for the last 10ka (Aucour et al., 1996). Using the fractionation coefficient (Aucour et al., 1996; Smith and Freeman, 2006; Feakins et al., 2016) and the

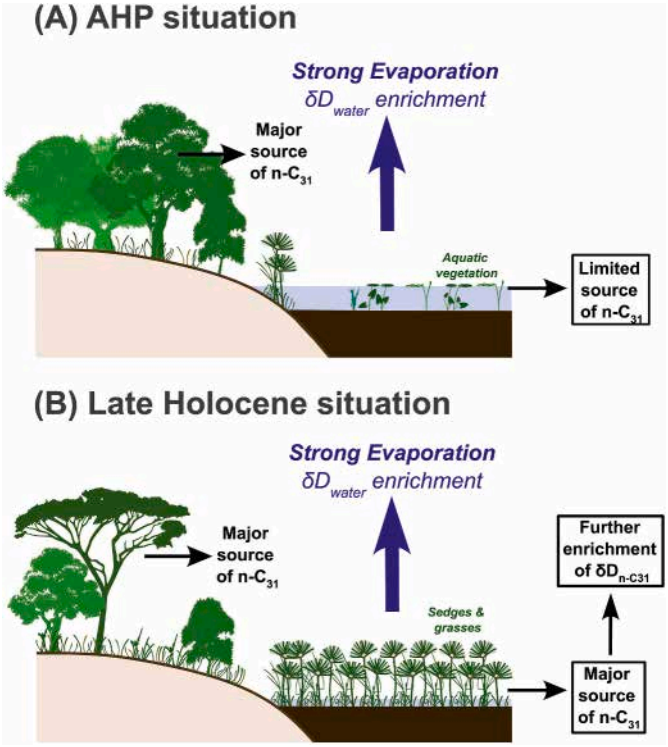

Fig. 9. Consequences of the changes in peatland vegetation on the range of measured δD values in leaf waxes.

global meteoric water line (Craig, 1961), this range in $\delta^{18}O_{cellulose}$ values would correspond to a range of around 60‰ in δD_{wax} (see supplementary material for more information on the method and its validation), well above the values observed in other African tropical lakes over the same period. In contrast, the Congo peat core analyzed by Garcin et al. (2022) shows an interval of δD_{wax} values of 33 and 26‰ for *n*-C_{29} and *n*-C_{31} alkanes, respectively. The Kyambangunguru and Kashiru peat deposits are nowadays dominated by sedges and grasses (Aucour et al., 1996; Coffinet et al., 2018), and pollen records at these two sites indicate significant environmental changes over the last 4 or 10 ka, respectively (Bonnefille and Riollet, 1988; Coffinet et al., 2018). The Congo peat core, on the other hand, is dominated by peat swamp forest, situated in a more equatorial region where the contrast between rainy and dry seasons and past environmental changes are much less marked than for the three other peat deposits presented above.

The δD_{wax} based on sedge-dominated peat deposits can therefore not be used to quantitatively record precipitation amounts, as the extent of variations can be affected by changes in local vegetation (Fig. 9). However, as peat records are particularly sensitive to climatic and environmental changes, such a record allows short- and long-term changes in precipitation amount or seasonality to be highlighted qualitatively by overexpressing them.

4.2.2. *Constrained hydroclimatic reconstruction at the Ngaoundaba peat deposit*

D-depleted $\delta D_{n\text{-}C31}$ values from 9.7 to 5.8 ka cal BP indicate wetter conditions (e.g., more precipitation or change in its seasonality) during the early to mid-Holocene consistent with the timing of the African Humid Period. The mid-Holocene is characterized by a progressive increase in the $\delta D_{n\text{-}C31}$ values (Fig. 10) suggesting a long-term drying trend, which associated with simultaneous autochthonous changes (i.e. sediment accumulation), triggered significant changes in wetland vegetation. The overall signal follows the insolation curve (Fig. 10). Up to 5.6 ka cal BP, the presence of semi-deciduous and montane taxa suggests a shorter dry season in the Ngaoundaba region. Between 8.9 and 7.8 ka cal BP, the $\delta D_{n\text{-}C31}$ values get heavier compared to the rest of the African Humid Period, which could indicate a diminution in precipitation or a change in its seasonality. This short "dry" event also

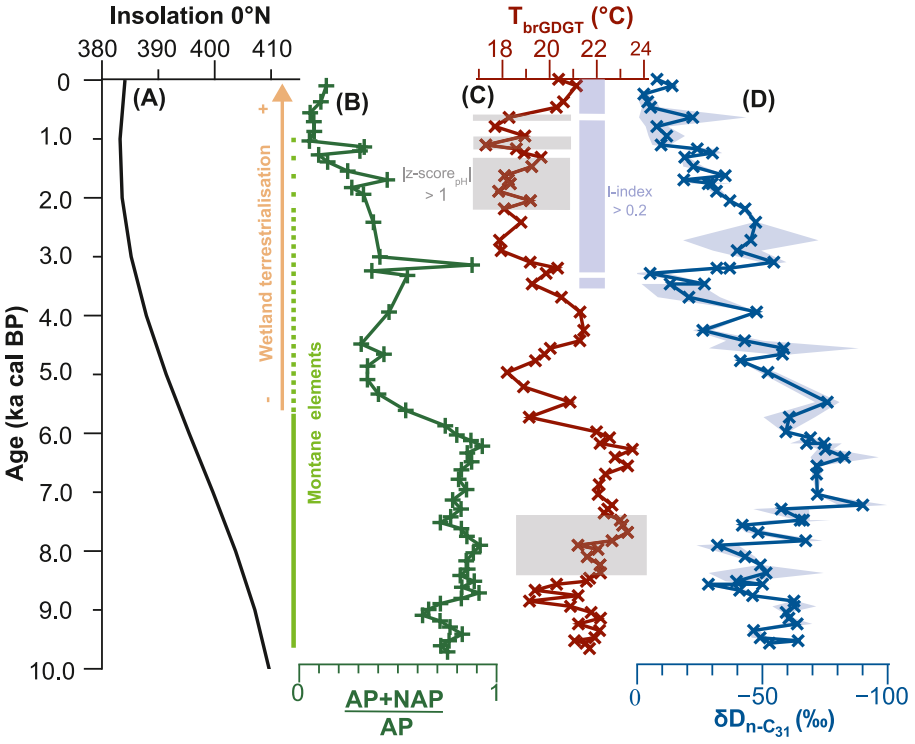

Fig. 10. Comparisons between pollen and geochemical data based on the Ngaoundaba peat record. (A) Insolation 0°N ($W.m^{-2}$) from Berger et al. (1981), (B) Arboreal over non-arboreal pollen ratio, (C) brGDGT-based temperature reconstruction based on the calibration from Dearing Crampton-Flood et al. (2020) and (D) $\delta D_{n\text{-}C31}$ corrected for vegetation changes.

impacted *in situ* vegetation with a highly variable signal in wetland vegetation during this period. This "dry" event is unevenly recorded $\delta D_{n\text{-}C29}$ and $\delta D_{n\text{-}C31}$ as well as between wetland and local vegetation, suggesting complex environmental changes during this period. From 5 to 3 ka cal BP, the $\delta D_{n\text{-}C31}$ values first get heavier to around 4-3.5 ka cal BP and then briefly get lighter around 3 ka cal BP before increasing until present. A marked increase in fern spore (Fig. 8) is recorded between around 4.5 to 3.5 ka indicating coeval changes in the local environment during this period, which is also seen in the pollen record from Mbi crater (Lézine et al., 2023).

4.3. Temperature record of the end of the AHP at Ngaoundaba based on GDGTs

4.3.1. Untangling influencing factors and temperature variations

To date, producers of brGDGTs remain poorly constrained (Halamka et al., 2023 and references therein). While the concentration of brGDGTs in peat usually increases with depth, suggesting a production by anaerobes (e.g., Weijers et al., 2009), some brGDGTs were detected in aerobic strains of Acidobacteria (Sinninghe Damsté et al., 2018) and incubation experiments suggest a greater production under oxic conditions (Huguet et al., 2017). The brGDGT-reconstructed temperature varies significantly during the past 1 ka, ranging from approximately 18 °C to as high as 21 °C (Fig. 4 D), well above the temperature variations expected during this period of time. The upper part of the record is marked by strong decomposition of the organic matter, reflected in the rapid increase of TOC values and the decrease in Rock-Eval® I-index which reflect thermolabile compounds (Schaaff et al., 2023) (Fig. 4 D). Therefore, during the last 3.5 ka cal BP (I-index >0.2), the brGDGT-reconstructed temperature values may be affected by strong microbial activity within the peat as a result of microbial degradation. Deeper in peat deposits, the brGDGTs are predominantly fossils (Weijers et al., 2011) and the impact of present-day microbial activity on brGDGT assemblages is likely limited.

The variation in temperature reconstructed from brGDGTs may be impacted, at the time of their production, by changes in other paleoparameters such as pH (De Jonge et al., 2019, 2021) or water saturation (Rao et al., 2022), inducing changes in the microbial community. Large pH variations (absolute values of pH_{brGDGT} z-score >2), highlighted in grey in Fig. 4 D, underline the periods during which temperature variations should be considered with caution.

Rao et al. (2022) proposed that about half of the temperature variation in three brGDGT-based Holocene temperature records from Chinese peats with contrasted environmental settings could result from changes in hydrology with a higher MBT'_{5Me} ratio in "dry" sites compared to "water" sites (Huguet et al., 2010; Rao et al., 2022). They further suggested a decoupling between air and water temperatures, water temperature being lower than air temperature in summer, or a difference in oxygen contents that could impact bacterial communities (Rao et al., 2022). On the contrary, in the Ngaoundaba peat deposit, high MBT'_{5Me} values and brGDGT-based temperatures are reconstructed during the wettest period and vice versa (Fig. 4). In tropical Africa, an alternative explanation could be a temperature decoupling between air and water, the latter being warmer, due to the high thermal capacity of water, similarly to what is modeled in lakes and consistent with measurements (Dee et al., 2018, 2021). This different water decoupling could explain the difference observed in MBT'_{5Me} between the Ngaoundaba peat deposit and peatlands analyzed in the study from Rao et al. (2022).

The Ngaoundaba peat deposit is marked by major changes in vegetation, with a decrease in arboreal pollen after 6-5 ka cal BP and the progressive terrestrialization of the peatland. It has been shown that vegetation changes in soils and lakes have an impact on brGDGT assemblages (Liang et al., 2019; Martin et al., 2019). In contrast to soils dominated by forest, lower levels of brGDGT-Ia were described in the soils dominated by reeds and grasslands of Lake Rotsee in Switzerland (Naeher et al., 2014), which is consistent with the changes observed at the Ngaoundaba peat deposit. Variations in vegetation may impact microbial communities (Too et al., 2018) and, in turn, brGDGT assemblages. Forested cover also limits erosion of the catchment area and the input of terrigenous brGDGTs to the wetland (Martin et al., 2019). When interpreting temperature reconstructed based on brGDGTs, the aforementioned confounding factors need to be considered as they can impact the variations in $T_{brGDGTs}$, particularly in terms of temperature range (Figs. 4 and 10).

4.3.2. Constrained temperature reconstruction at the Ngaoundaba peat deposit

The temperature values during the early Holocene are similar to present-day mean annual air temperature, which is consistent with other records (Powers et al., 2005; Baxter et al., 2023). While proxy-based records in Africa typically anticipate a warming of up to 2 °C during the mid-Holocene (8-5 ka) compared to the preindustrial period (Powers et al., 2005; Berke et al., 2012), models generally predict minimal warming or even a slight cooling in the intertropical zone (Kaufman and Broadman, 2023; Marshall et al., 2024 and references therein). Between 8 and 5.7 ka cal BP, the brGDGT-temperature recorded in the Ngaoundaba peat ranges from 22.0 to 23.5 °C, which is higher than the temperature recorded during the late Holocene, supporting a slight increase in temperature during the mid-Holocene compared to the preindustrial period.

A sharp drop in temperature of approximately 4 °C is recorded around 5.7 ka cal BP. This large range of temperature variations can probably be explained by the significant changes in precipitation and vegetation that occurred simultaneously (Fig. 10). Temperature remained low during most of the middle and late Holocene, suggesting the influence of confounding factors. The temperature minimum around 5 ka cal BP could be a long-lasting consequence of the abrupt change observed around 5.7 ka cal BP. In the section of the core corresponding to the late Holocene, the low T_{brGDGT} values coincide with high values of the I-index suggesting active microbial degradation that could affect brGDGT-producing microbial community (Fig. 10).

Changes in T_{brGDGT} are partially decoupled with changes in $\delta D_{n\text{-alk}}$ (Fig. 10). The decrease in temperature recorded between 8.9 and 8.5 ka cal BP cannot be explained solely by changes in precipitation amount and/or seasonality, as the $\delta D_{n\text{-alk}}$ values get heavier during this period, but the period of heavier $\delta D_{n\text{-alk}}$ values lasts until 7.9 ka cal BP. On the contrary, between 3.5 and 4.5 ka cal BP, the temperature increase recorded in T_{brGDGT} values coincides with more D-enriched $\delta D_{n\text{-alk}}$ values.

4.4. An integrated picture of the end of the AHP in Central West Africa

Cluster analyses of the Ngaoundaba peat records consistently indicate a significant climatic transition that occurred around 5.7–5.6 ka cal BP (Fig. 7). Prior to this period, from the bottom of the core to approximately 5.7–5.6 ka cal BP, the region experienced a wetter and warmer climate, which favored the development of a floristically complex forest environment characterized by seasonal and evergreen forest taxa. Elevated peat water levels during this period helped to create an open water environment, favoring the development of shoreline and aquatic vegetation, along with phases where grasses and sedges expanded. Changes in forest taxa are reported as early as 6.1 ka cal BP, which is consistent with pollen records from nearby Lake Mbalang (Vincens et al., 2010). Despite a distance of only 25 km, the forest regrowth recorded at Lake Mbalang between 5.2 and 4.2 ka cal BP does not coincide with the decrease in arboreal taxa observed at Ngaoundaba. The increase in grass and sedge pollen after 5.6 ka cal BP suggests a gradual terrestrialization of the peatland, while the progressive decline in the abundance and diversity of arboreal pollen indicates a shift from a forest landscape to a wooded savanna. At both Mbalang and Ngaoundaba, the persistence of *Olea capensis* up to 3 to 2 ka cal BP is likely

linked to the altitudinal position of these sites, as well as to potentially shorter dry seasons or variations in cloud cover compared to present-day conditions. Consistent with $\delta D_{n\text{-alk}}$ records from lakes Barombi and Bosumtwi, the $\delta D_{n\text{-alk}}$ from Ngaoundaba records the African Humid Period and the transition toward drier conditions during the middle and late Holocene. However, while the records from lake Barombi closely follow insolation changes, the Ngaoundaba peat record is affected by several short and abrupt 'dry' events. Oscillations between an open water and vegetation-covered wetland indicated that this site's hydrology is particularly sensitive to climate changes compared to lakes. These climatic changes may have triggered significant changes in the local vegetation, affecting both pollen and lipid biomarker records. Alternatively, the position of the Ngaoundaba peat deposit in a wooded savanna zone, at the transition between the semi-deciduous forest zone and the savanna-woodland zone, may be particularly susceptible to short-term changes in climatic conditions. Several major hydroclimatic features emerge from the West and Central $\delta D_{n\text{-alk}}$ records. Firstly, a first-order signal closely follows changes in insolation during the Holocene, with a global decreasing trend between the early and late Holocene. The record of lake Barombi perfectly illustrates this trend (Garcin et al., 2018), a pattern observed across all sites in West and Central Africa. Secondly, major vegetation changes occurred during the mid-Holocene (e.g., Giresse et al., 1994; Ngomanda et al., 2009; Vincens et al., 2010, this study). The more abrupt changes observed at some sites (Collins et al., 2017, this study) may be explained by vegetation feedbacks, the influence of which may have depended on the initial vegetation composition (e.g., Hély et al., 2009; Claussen et al., 2017). Lastly, the Ngaoundaba peat record highlights several short events that are likely disconnected from the insolation changes. The sensitivity of each site depends on numerous environmental parameters such as wetland types, latitudinal and altitudinal position, vegetation stability, and hydrogeomorphic factors (e.g. catchment size). Similarly, a short drought episode might also have affected the GeoB9508-5 marine records located off the coast of Senegal (Niedermeyer et al., 2010) around 8-7 ka cal BP, while a wet episode centered around 5-4 ka cal BP possibly affected the $\delta D_{n\text{-alk}}$ record from lake Bosumtwi (Shanahan et al., 2015).

5. Conclusion

Understanding the end of the AHP in Central West Africa has proven challenging, ranging from an abrupt end in a few decades to centuries (DeMenocal et al., 2000) to a progressive termination closely following insolation changes (Garcin et al., 2018). The significant differences between proxies and sites are often complicated by uncertainties in age models. This study provides a new continuous, multi-proxy, high--resolution paleoenvironmental and paleoclimatic record in northern Cameroon, spanning most of the Holocene and specifically documenting the end of the African Humid Period. All pollen and lipid biomarker proxies indicate a transition occurring approximately between 5.7 and 5.6 ka cal BP. From 9.7 to 5.7-5.6 ka cal BP, microbial lipid biomarkers indicate low oxygen availability in the sediment, while bulk analyses demonstrate effective preservation of organic matter. This period was characterized by a wetter and warmer climate that favored the development of a closed forest comprising semi-deciduous and evergreen taxa, alongside an open water environment. After 5.7-5.6 ka cal BP, a decrease in total precipitation and/or changes in seasonality led to modifications in regional and local wetland vegetation. The decline of the water table resulted in the gradual terrestrialization of the peat, as evidenced by the peak in fern spores and subsequent rise in grass and sedge pollens accompanying ^{13}C-enriched $\delta^{13}C_{n\text{-alk}}$ values. Multiple brief 'dry' events are documented around 9-8 ka and 4.5-3.5 ka cal BP, marked by less D-depleted $\delta D_{n\text{-alk}}$ values and significant variations in T_{brGDGT}, as well as bulk organic proxies like HI and local wetland vegetation.

The configuration of the Ngaoundaba site makes it highly vulnerable to hydrological changes, resulting in possibly rapid switches between open water and a vegetated wetland. This specificity, combined with its latitudinal position in the Sudano-Guinean vegetation zone, makes it particularly sensitive to capturing short-term, transient climatic and environmental variations. The Ngaoundaba peat record documents significant regional climatic and environmental changes, as well as substantial alterations in local wetland vegetation and peat functioning. As shown in this study, a multi-proxy approach comparing the responses of proxies that are variably influenced by autogenic changes may help disentangle the regional from the *in situ* forcing.

At this stage, it remains difficult to identify the potential influence of human activities in the Ngaoundaba peat sequence. The impact of pastoralism, agriculture, or metallurgy on sub-Saharan ecosystems during the AHP transition remains a subject of debate (Wright, 2017; Brierley et al., 2018). On the Adamawa plateau, archaeological investigations are too limited to provide a global overview of human occupation and activities in the region as it was done for the forest block to the south (de Saulieu et al., 2021). However, the pioneering work from Zangato and Holl (2010) suggests iron production on the eastern edge of the Adamawa plateau (situated at 150 km away from the Ngaoundaba peat deposit) dating back to approximately 4 ka cal BP, and possibly as early as 5 ka cal BP. The acquisition of new sedimentary records, specifically lacustrine sequences spanning the entirety of the Holocene, in conjunction with additional archaeological investigations, will be valuable for evaluating the local or regional nature of climatic, environmental, and vegetational changes and potentially clarifying the influence of human activities, including slash-and-burn cultivation and metallurgy, in a region that plays a key role in the transition between the Sahelian and Guineo-Congolian zones.

CRediT authorship contribution statement

Valentine Schaaff: Conceptualization, Investigation, Formal analysis, Data curation, Writing – original draft, Writing – review & editing. **Vincent Grossi:** Conceptualization, Resources, Writing – original draft, Writing – review & editing, Supervision, Funding acquisition. **Matthew Makou:** Writing – review & editing, Supervision. **Yannick Garcin:** Writing – review & editing, Resources. **Pierre Deschamps:** Writing – review & editing, Resources. **Bruno Hamelin:** Writing – review & editing, Resources. **Christopher A. Kiahtipes:** Investigation, Formal analysis, Data curation, Writing – original draft, Writing – review & editing. **David Sebag:** Writing – review & editing. **Benjamin Ngounou Ngatcha:** Writing – review & editing, Resources. **Guillemette Ménot:** Conceptualization, Resources, Writing – original draft, Writing – review & editing, Supervision, Funding acquisition.

Declaration of competing interest

The authors declare that they have no known competing financial interests or personal relationships that could have appeared to influence the work reported in this paper.

Acknowledgments

This work was funded by the ANR project TAPIOCA (ANR-18-CE01-0005) granted to G. Ménot. The ENS de Lyon financed the PhD scholarship of V. Schaaff. Radiocarbon dating has been supported through the French CNRS-INSU-IRD Radiocarbon program (France) and performed at the LMC14 laboratory with the ARTEMIS facility in Saclay. We thank A.C. Van Aardt and an anonymous reviewer for their constructive comments. We thank S. Ansanay-Alex, I. Antheaume and B. Eddhif for laboratory assistance. This work was carried out within the frame of the LMI DYCOFAC supported by French National Research Institute for Sustainable Development (IRD) and the CALAKÉ project supported by the Labex OT-Med (project ANR-11-LABEX-0061). We are grateful to IRD Cameroon for its logistic support.

Appendix A. Supplementary data

Supplementary data to this article can be found online at https://doi.org/10.1016/j.quascirev.2025.109307.

Data availability

Data can be downloaded at: https://doi.org/10.1594/PANGAEA.979862, https://doi.org/10.1594/PANGAEA.979861 (brGDGT data), https://doi.org/10.1594/PANGAEA.979863 (isotopic data) and https://doi.org/10.1594/PANGAEA.979864 (pollen data).

References

Abba, S., Hamelin, B., Michelot, J.-L., Garcin, Y., Deschamps, P., 2023. Water budget of tropical volcanic lakes in center-north Cameroon: reconciling the stable isotope and chloride mass balance. Hydrol. Process. 37, e14923.

Adkins, J., deMenocal, P., Eshel, G., 2006. The "African humid period" and the record of marine upwelling from excess 230Th in Ocean Drilling Program Hole 658C. Paleoceanography 21.

Aucour, A.-M., Hillaire-Marcel, C., Bonnefille, R., 1996. Oxygen isotopes in cellulose from modern and quaternary intertropical peatbogs: implications for palaeohydrology. Chem. Geol. 129, 341–359.

Baxter, A.J., Verschuren, D., Peterse, F., Miralles, D.G., Martin-Jones, C.M., Maitituerdi, A., Van der Meeren, T., Van Daele, M., Lane, C.S., Haug, G.H., Olago, D. O., Sinninghe Damsté, J.S., 2023. Reversed Holocene temperature–moisture relationship in the horn of Africa. Nature 620, 336–343.

Berger, A., Guiot, J., Kukla, G., Pestiaux, P., 1981. Long-term variations of monthly insolation as related to climatic changes. Geol. Rundsch. 70, 748–758.

Berke, M.A., Johnson, T.C., Werne, J.P., Schouten, S., Sinninghe Damsté, J.S., 2012. A mid-Holocene thermal maximum at the end of the African Humid Period. Earth Planet Sci. Lett. 351–352, 95–104.

Bonnefille, R., Riollet, G., 1988. The Kashiru pollen sequence (Burundi) palaeoclimatic implications for the last 40,000 yr B.P. In tropical Africa. Quat. Res. 30, 19–35.

Brierley, C., Manning, K., Maslin, M., 2018. Pastoralism may have delayed the end of the green Sahara. Nat. Commun. 9, 4018.

Claussen, M., Dallmeyer, A., Bader, J., 2017. Theory and Modeling of the African Humid Period and the Green Sahara.

Claussen, M., Kubatzki, C., Brovkin, V., Ganopolski, A., Hoelzmann, P., Pachur, H.-J., 1999. Simulation of an abrupt change in Saharan vegetation in the Mid-Holocene. Geophys. Res. Lett. 26, 2037–2040.

Coffinet, S., Huguet, A., Bergonzini, L., Pedentchouk, N., Williamson, D., Anquetil, C., Gałka, M., Kołaczek, P., Karpińska-Kołaczek, M., Majule, A., Laggoun-Défarge, F., Wagner, T., Derenne, S., 2018. Impact of climate change on the ecology of the Kyambangunguru crater marsh in southwestern Tanzania during the Late Holocene. Quat. Sci. Rev. 196, 100–117.

Collins, J.A., Prange, M., Caley, T., Gimeno, L., Beckmann, B., Mulitza, S., Skonieczny, C., Roche, D., Schefuß, E., 2017. Rapid termination of the African Humid Period triggered by northern high-latitude cooling. Nat. Commun. 8, 1372.

Collister, J.W., Rieley, G., Stern, B., Eglinton, G., Fry, B., 1994. Compound-specific δ 13C analyses of leaf lipids from plants with differing carbon dioxide metabolisms. Org. Geochem. 21, 619–627.

Craig, H., 1961. Isotopic variations in meteoric waters. Science 133, 1702–1703.

Dallmeyer, A., Claussen, M., Lorenz, S.J., Shanahan, T., 2020. The end of the African humid period as seen by a transient comprehensive Earth system model simulation of the last 8000 years. Clim. Past 16, 117–140.

De Jonge, C., Hopmans, E.C., Zell, C.I., Kim, J.-H., Schouten, S., Sinninghe Damsté, J.S., 2014. Occurrence and abundance of 6-methyl branched glycerol dialkyl glycerol tetraethers in soils: implications for palaeoclimate reconstruction. Geochem. Cosmochim. Acta 141, 97–112.

De Jonge, C., Kuramae, E.E., Radujković, D., Weedon, J.T., Janssens, I.A., Peterse, F., 2021. The influence of soil chemistry on branched tetraether lipids in mid- and high latitude soils: implications for brGDGT- based paleothermometry. Geochem. Cosmochim. Acta 310, 95–112.

De Jonge, C., Radujković, D., Sigurdsson, B.D., Weedon, J.T., Janssens, I., Peterse, F., 2019. Lipid biomarker temperature proxy responds to abrupt shift in the bacterial community composition in geothermally heated soils. Org. Geochem. 137, 103897.

de Saulieu, G., Garcin, Y., Sebag, D., Nlend, P.R., Zeitlyn, D., Deschamps, P., Ménot, G., Di Carlo, P., Oslisly, R., 2021. Archaeological evidence for population rise and collapse between ~2500 and ~500 cal. Yr BP in western central Africa. aaa 17, 11–32.

Dearing Crampton-Flood, E., Tierney, J.E., Peterse, F., Kirkels, F.M.S.A., Sinninghe Damsté, J.S., 2020. BayMBT: a Bayesian calibration model for branched glycerol dialkyl glycerol tetraethers in soils and peats. Geochem. Cosmochim. Acta 268, 142–159.

Dee, S.G., Morrill, C., Kim, S.H., Russell, J.M., 2021. Hot air, hot lakes, or both? Exploring mid-holocene african temperatures using proxy system modeling. J. Geophys. Res. Atmos. 126, e2020JD033269.

Dee, S.G., Russell, J.M., Morrill, C., Chen, Z., Neary, A., 2018. PRYSM v2.0: a proxy system model for lacustrine archives. Paleoceanogr. Paleoclimatol. 33, 1250–1269.

Delalande, M., Bergonzini, L., Massault, M., 2008. Mbaka lakes isotopic (18O and 2H) and water balances: discussion on the used atmospheric moisture compositions. Isot. Environ. Health Stud. 44, 71–82.

DeMenocal, P., Ortiz, J., Guilderson, T., Adkins, J., Sarnthein, M., Baker, L., Yarusinsky, M., 2000. Abrupt onset and termination of the African Humid Period: rapid climate responses to gradual insolation forcing. Quat. Sci. Rev. 19, 347–361.

Feakins, S.J., Bentley, L.P., Salinas, N., Shenkin, A., Blonder, B., Goldsmith, G.R., Ponton, C., Arvin, L.J., Wu, M.S., Peters, T., West, A.J., Martin, R.E., Enquist, B.J., Asner, G.P., Malhi, Y., 2016. Plant leaf wax biomarkers capture gradients in hydrogen isotopes of precipitation from the Andes and Amazon. Geochem. Cosmochim. Acta 182, 155–172.

Ficken, K.J., Li, B., Swain, D.L., Eglinton, G., 2000. An n-alkane proxy for the sedimentary input of submerged/floating freshwater aquatic macrophytes. Org. Geochem. 31, 745–749.

Francey, R.J., Allison, C.E., Etheridge, D.M., Trudinger, C.M., Enting, I.G., Leuenberger, M., Langenfelds, R.L., Michel, E., Steele, L.P., 1999. A 1000-year high precision record of δ13C in atmospheric CO2. Tellus B 51, 170–193.

Garcin, Y., Deschamps, P., Ménot, G., De Saulieu, G., Schefuß, E., Sebag, D., Dupont, L. M., Oslisly, R., Brademann, B., Mbusnum, K.G., Onana, J.-M., Ako, A.A., Epp, L.S., Tjallingii, R., Strecker, M.R., Brauer, A., Sachse, D., 2018. Early anthropogenic impact on Western Central African rainforests 2,600 y ago. Proceedings of the National Academy of Sciences USA 115, 3261–3266.

Garcin, Y., Schefuß, E., Dargie, G.C., Hawthorne, D., Lawson, I.T., Sebag, D., Biddulph, G. E., Crezee, B., Bocko, Y.E., Ifo, S.A., Mampouya Wenina, Y.E., Mbemba, M., Ewango, C.E.N., Emba, O., Bola, P., Kanyama Tabu, J., Tyrrell, G., Young, D.M., Gassier, G., Girkin, N.T., Vane, C.H., Adatte, T., Baird, A.J., Boom, A., Gulliver, P., Morris, P.J., Page, S.E., Sjögersten, S., Lewis, S.L., 2022. Hydroclimatic vulnerability of peat carbon in the central Congo Basin. Nature 1–6.

Garcin, Y., Schefuß, E., Schwab, V.F., Garreta, V., Gleixner, G., Vincens, A., Todou, G., Séné, O., Onana, J.-M., Achoundong, G., Sachse, D., 2014. Reconstructing C3 and C4 vegetation cover using n-alkane carbon isotope ratios in recent lake sediments from Cameroon, Western Central Africa. Geochem. Cosmochim. Acta 142, 482–500.

Gibson, J.J., Edwards, T.W.D., 2002. Regional water balance trends and evaporation-transpiration partitioning from a stable isotope survey of lakes in northern Canada. Glob. Biogeochem. Cycles 16, 10–11.

Giresse, P., Maley, J., Brenac, P., 1994. Late Quaternary palaeoenvironments in the Lake Barombi Mbo (West Cameroon) deduced from pollen and carbon isotopes of organic matter. Palaeogeogr. Palaeoclimatol. Palaeoecol. 107, 65–78.

Griepentrog, M., De Wispelaere, L., Bauters, M., Bodé, S., Hemp, A., Verschuren, D., Boeckx, P., 2019. Influence of plant growth form, habitat and season on leaf-wax n-alkane hydrogen-isotopic signatures in equatorial East Africa. Geochem. Cosmochim. Acta 263, 122–139.

Halamka, T.A., Raberg, J.H., McFarlin, J.M., Younkin, A.D., Mulligan, C., Liu, X.-L., Kopf, S.H., 2023. Production of diverse brGDGTs by Acidobacterium Solibacter usitatus in response to temperature, pH, and O2 provides a culturing perspective on brGDGT proxies and biosynthesis. Geobiology 21, 102–118.

Harris, I., Jones, P.D., Osborn, T.J., Lister, D.H., 2014. Updated high-resolution grids of monthly climatic observations–the CRU TS3. 10 Dataset. Int. J. Climatol. 34, 623–642.

Hély, C., Braconnot, P., Watrin, J., Zheng, W., 2009. Climate and vegetation: simulating the African humid period. C. R. Geosci. 341, 671–688.

Hopmans, E.C., Schouten, S., Damsté, J.S.S., 2016. The effect of improved chromatography on GDGT-based palaeoproxies. Org. Geochem. 93, 1–6.

Huguet, A., Fosse, C., Laggoun-Défarge, F., Toussaint, M.-L., Derenne, S., 2010. Occurrence and distribution of glycerol dialkyl glycerol tetraethers in a French peat bog. Org. Geochem. 41, 559–572.

Huguet, A., Meador, T.B., Laggoun-Défarge, F., Könneke, M., Wu, W., Derenne, S., Hinrichs, K.-U., 2017. Production rates of bacterial tetraether lipids and fatty acids in peatland under varying oxygen concentrations. Geochem. Cosmochim. Acta 203, 103–116.

Huguet, C., Hopmans, E.C., Febo-Ayala, W., Thompson, D.H., Sinninghe Damsté, J.S., Schouten, S., 2006. An improved method to determine the absolute abundance of glycerol dibiphytanyl glycerol tetraether lipids. Org. Geochem. 37, 1036–1041.

Juggins, S., Juggins, M.S., 2019. Package 'rioja.

Kaufman, D.S., Broadman, E., 2023. Revisiting the Holocene global temperature conundrum. Nature 614, 425–435.

Keeling, C.D., 1979. The Suess effect: 13Carbon-14Carbon interrelations. Environ. Int. 2, 229–300.

Killops, V.J., Killops, S.D., 2013. Introduction to Organic Geochemistry. John Wiley & Sons.

Kristen, I., Wilkes, H., Vieth, A., Zink, K.-G., Plessen, B., Thorpe, J., Partridge, T.C., Oberhänsli, H., 2010. Biomarker and stable carbon isotope analyses of sedimentary organic matter from Lake Tswaing: evidence for deglacial wetness and early Holocene drought from South Africa. J. Paleolimnol. 44, 143–160.

Kutzbach, J., Bonan, G., Foley, J., Harrison, S.P., 1996. Vegetation and soil feedbacks on the response of the African monsoon to orbital forcing in the early to middle Holocene. Nature 384, 623–626.

Lebamba, J., Vincens, A., Lézine, A.-M., Marchant, R., Buchet, G., 2016. Forest-savannah dynamics on the Adamawa plateau (Central Cameroon) during the "African humid period" termination: a new high-resolution pollen record from Lake Tizong. Rev. Palaeobot. Palynol. 235, 129–139.

Lehtonen, K., Ketola, M., 1993. Solvent-extractable lipids of Sphagnum, Carex, Bryales and Carex-Bryales peats: content and compositional features vs peat humification. Org. Geochem. 20, 363–380.

Letouzey, R., 1958. Phytogéographie camerounaise. In: Atlas du Cameroun. IRCAM, Yaoundé, p. 6.

Letouzey, R., 1985. Notice de la carte phytogeographique du Cameroun au 1, 500,000 (1985).
Lézine, A.-M., 2017. Vegetation at the time of the african Humid Period. In: Oxford Research Encyclopedia of Climate Science.
Lézine, A.-M., Izumi, K., Achoundong, G., 2023. Mbi Crater (Cameroon) illustrates the relations between mountain and lowland forests over the past 15,000 years in western equatorial Africa. Quat. Int. 657, 67–76.
Lézine, A.-M., Lemonnier, K., Waller, M.P., Bouimetarhan, I., Dupont, L., 2021. Changes in the West african landscape at the end of the african Humid Period. In: Quaternary Vegetation Dynamics. CRC Press, pp. 65–84.
Liang, J., Russell, J.M., Xie, H., Lupien, R.L., Si, G., Wang, J., Hou, J., Zhang, G., 2019. Vegetation effects on temperature calibrations of branched glycerol dialkyl glycerol tetraether (brGDGTs) in soils. Org. Geochem. 127, 1–11.
Lytle, T.F., Lytle, J.S., Caruso, A., 1976. Hydrocarbons and fatty acids of ferns. Phytochemistry 15, 965–970.
Marshall, C., Morrill, C., Dee, S., Pausata, F.S.R., Russell, J., 2024. Causes of past african temperature change in PMIP simulations of the mid-holocene. Paleoceanogr. Paleoclimatol. 39, e2023PA004706.
Martin, C., Ménot, G., Thouveny, N., Davtian, N., Andrieu-Ponel, V., Reille, M., Bard, E., 2019. Impact of human activities and vegetation changes on the tetraether sources in Lake St Front (Massif Central, France). Org. Geochem. 135, 38–52.
Martínez-Sosa, P., Tierney, J.E., Stefanescu, I.C., Dearing Crampton-Flood, E., Shuman, B.N., Routson, C., 2021. A global Bayesian temperature calibration for lacustrine brGDGTs. Geochem. Cosmochim. Acta 305, 87–105.
Marzi, R., Torkelson, B.E., Olson, R.K., 1993. A revised carbon preference index. Org. Geochem. 20, 1303–1306.
McCarroll, D., Loader, N.J., 2004. Stable isotopes in tree rings. Quat. Sci. Rev. 23, 771–801.
Miller, D.R., Habicht, M.H., Keisling, B.A., Castañeda, I.S., Bradley, R.S., 2018. A 900-year New England temperature reconstruction from in situ seasonally produced branched glycerol dialkyl glycerol tetraethers (brGDGTs). Clim. Past 14, 1653–1667.
Naafs, B.D.A., Inglis, G.N., Zheng, Y., Amesbury, M.J., Biester, H., Bindler, R., Blewett, J., Burrows, M.A., Del Castillo Torres, D., Chambers, F.M., 2017. Introducing global peat-specific temperature and pH calibrations based on brGDGT bacterial lipids. Geochem. Cosmochim. Acta 208, 285–301.
Naeher, S., Peterse, F., Smittenberg, R.H., Niemann, H., Zigah, P.K., Schubert, C.J., 2014. Sources of glycerol dialkyl glycerol tetraethers (GDGTs) in catchment soils, water column and sediments of Lake Rotsee (Switzerland) – implications for the application of GDGT-based proxies for lakes. Org. Geochem. 66, 164–173.
Ngomanda, A., Neumann, K., Schweizer, A., Maley, J., 2009. Seasonality change and the third millennium BP rainforest crisis in southern Cameroon (Central Africa). Quat. Res. 71, 307–318.
Ngos, S., Giresse, P., 2012. The Holocene sedimentary and pyroclastic accumulations of two crater lakes (Mbalang,Tizong) of the volcanic plateau of Adamawa (Cameroon): palaeoenvironmental reconstruction. Holocene 22, 31–42.
Nguetsop, V.F., Bentaleb, I., Favier, C., Martin, C., Bietrix, S., Giresse, P., Servant-Vildary, S., Servant, M., 2011. Past environmental and climatic changes during the last 7200 cal yr BP in Adamawa plateau (Northern-Cameroun) based on fossil diatoms and sedimentary carbon isotopic records from Lake Mbalang. Clim. Past 7, 1371–1393.
Nguetsop, V.F., Bentaleb, I., Favier, C., Bietrix, S., Martin, C., Servant-Vildary, S., Servant, M., 2013. A late Holocene palaeoenvironmental record from Lake Tizong, northern Cameroon using diatom and carbon stable isotope analyses. Quat. Sci. Rev. 72, 49–62.
Nichols, J.E., Booth, R.K., Jackson, S.T., Pendall, E.G., Huang, Y., 2006. Paleohydrologic reconstruction based on n-alkane distributions in ombrotrophic peat. Org. Geochem. 37, 1505–1513.
Niedermeyer, E.M., Schefuß, E., Sessions, A.L., Mulitza, S., Mollenhauer, G., Schulz, M., Wefer, G., 2010. Orbital- and millennial-scale changes in the hydrologic cycle and vegetation in the western African Sahel: insights from individual plant wax δD and δ13C. Quat. Sci. Rev. 29, 2996–3005.
Oksanen, J., Blanchet, F.G., Kindt, R., Legendre, P., Minchin, P.R., O'hara, R., Simpson, G.L., Solymos, P., Stevens, M.H.H., Wagner, H., 2013. Package 'vegan.' Community Ecology Package, pp. 1–295, version 2.
Pausata, F.S., Gaetani, M., Messori, G., Berg, A., de Souza, D.M., Sage, R.F., DeMenocal, P.B., 2020. The greening of the Sahara: past changes and future implications. One Earth 2, 235–250.
Powers, L.A., Johnson, T.C., Werne, J.P., Castañeda, I.S., Hopmans, E.C., Sinninghe Damsté, J.S., Schouten, S., 2005. Large temperature variability in the southern african tropics since the last glacial maximum. Geophys. Res. Lett. 32.
Poynter, J., Eglinton, G., 1990. 14. Molecular composition of three sediments from hole 717c: the Bengal fan. In: Proceedings of the Ocean Drilling Program. Scientific Results, pp. 155–161.
Poynter, J.G., Farrimond, P., Robinson, N., Eglinton, G., 1989. Aeolian-derived higher plant lipids in the marine sedimentary record: links with palaeoclimate. In: Leinen, M., Sarnthein, M. (Eds.), Paleoclimatology and Paleometeorology: Modern and Past Patterns of Global Atmospheric Transport. Springer, Netherlands, Dordrecht, pp. 435–462.
Rao, Z., Guo, H., Wei, S., Cao, J., Jia, G., 2022. Influence of water conditions on peat brGDGTs: a modern investigation and its paleoclimatic implications. Chem. Geol. 606, 120993.
Renssen, H., Brovkin, V., Fichefet, T., Goosse, H., 2006. Simulation of the Holocene climate evolution in northern Africa: the termination of the african Humid Period. Quat. Int. 150, 95–102.
Rommerskirchen, F., Plader, A., Eglinton, G., Chikaraishi, Y., Rullkötter, J., 2006. Chemotaxonomic significance of distribution and stable carbon isotopic composition of long-chain alkanes and alkan-1-ols in C4 grass waxes. Org. Geochem. 37, 1303–1332.
Rubino, M., Etheridge, D.M., Trudinger, C.M., Allison, C.E., Battle, M.O., Langenfelds, R. L., Steele, L.P., Curran, M., Bender, M., White, J.W.C., Jenk, T.M., Blunier, T., Francey, R.J., 2013. A revised 1000 year atmospheric δ13C-CO2 record from Law Dome and South Pole, Antarctica. J. Geophys. Res. Atmos. 118, 8482–8499.
Sachse, D., Billault, I., Bowen, G.J., Chikaraishi, Y., Dawson, T.E., Feakins, S.J., Freeman, K.H., Magill, C.R., McInerney, F.A., Van Der Meer, M.T.J., Polissar, P., Robins, R.J., Sachs, J.P., Schmidt, H.-L., Sessions, A.L., White, J.W.C., West, J.B., Kahmen, A., 2012. Molecular paleohydrology: interpreting the hydrogen-isotopic composition of lipid biomarkers from photosynthesizing organisms. Annu. Rev. Earth Planet Sci. 40, 221–249.
Salzmann, U., Hoelzmann, P., Morczinek, I., 2002. Late quaternary climate and vegetation of the sudanian zone of Northeast Nigeria. Quat. Res. 58, 73–83.
Schaaff, V., Grossi, V., Makou, M., Garcin, Y., Deschamps, P., Sebag, D., Ngounou Ngatcha, B., Ménot, G., 2024. Constraints on hopanes and brGDGTs as pH proxies in peat. Geochem. Cosmochim. Acta 373, 342–354.
Schaaff, V., Sebag, D., Makou, M., Grossi, V., Antheaume, I., Hamelin, B., Garcin, Y., Ngounou Ngatcha, B., Deschamps, P., Ménot, G., 2023. Modeling the decomposition signal and correcting bulk organic data from a peat deposit, a case study at low latitudes (Cameroon). Org. Geochem. 179, 104589.
Schefuß, E., Schouten, S., Schneider, R.R., 2005. Climatic controls on central African hydrology during the past 20,000 years. Nature 437, 1003–1006.
Shanahan, T.M., McKay, N.P., Hughen, K.A., Overpeck, J.T., Otto-Bliesner, B., Heil, C.W., King, J., Scholz, C.A., Peck, J., 2015. The time-transgressive termination of the african Humid Period. Nat. Geosci. 8, 140–144.
Shanahan, T.M., Overpeck, J.T., Wheeler, C.W., Beck, J.W., Pigati, J.S., Talbot, M.R., Scholz, C.A., Peck, J., King, J.W., 2006. Paleoclimatic variations in West Africa from a record of late pleistocene and Holocene lake level stands of Lake Bosumtwi, Ghana. Palaeogeogr. Palaeoclimatol. Palaeoecol. 242, 287–302.
Sinninghe Damsté, J.S., Rijpstra, W.I.C., Foesel, B.U., Huber, K.J., Overmann, J., Nakagawa, S., Kim, J.J., Dunfield, P.F., Dedysh, S.N., Villanueva, L., 2018. An overview of the occurrence of ether- and ester-linked iso-diabolic acid membrane lipids in microbial cultures of the Acidobacteria: implications for brGDGT paleoproxies for temperature and pH. Org. Geochem. 124, 63–76.
Smith, F.A., Freeman, K.H., 2006. Influence of physiology and climate on δD of leaf wax n-alkanes from C3 and C4 grasses. Geochem. Cosmochim. Acta 70, 1172–1187.
Tierney, J.E., Pausata, F.S.R., deMenocal, P.B., 2017. Rainfall regimes of the green sahara. Sci. Adv. 3, e1601503.
Too, C.C., Keller, A., Sickel, W., Lee, S.M., Yule, C.M., 2018. Microbial community structure in a Malaysian tropical peat swamp forest: the influence of tree species and depth. Front. Microbiol. 9, 2859.
Véquaud, P., Thibault, A., Derenne, S., Anquetil, C., Collin, S., Contreras, S., Nottingham, A.T., Sabatier, P., Werne, J.P., Huguet, A., 2022. FROG: a global machine-learning temperature calibration for branched GDGTs in soils and peats. Geochem. Cosmochim. Acta 318, 468–494.
Vincens, A., Buchet, G., Servant, M., ECOFIT Mbalang collaborators, 2010. Vegetation response to the "African Humid Period" termination in Central Cameroon (7° N)–new pollen insight from Lake Mbalang. Clim. Past 6, 281–294.
Vogts, A., Moossen, H., Rommerskirchen, F., Rullkötter, J., 2009. Distribution patterns and stable carbon isotopic composition of alkanes and alkan-1-ols from plant waxes of African rain forest and savanna C3 species. Org. Geochem. 40, 1037–1054.
Watrin, J., Lézine, A.-M., Gajewski, K., Vincens, A., 2007. Pollen–plant–climate relationships in sub-Saharan Africa. J. Biogeogr. 34, 489–499.
Weijers, J.W.H., Panoto, E., van Bleijswijk, J., Schouten, S., Rijpstra, W.I.C., Balk, M., Stams, A.J.M., Damsté, J.S.S., 2009. Constraints on the biological source(s) of the orphan branched tetraether membrane lipids. Geomicrobiol. J. 26, 402–414.
Weijers, J.W.H., Steinmann, P., Hopmans, E.C., Schouten, S., Sinninghe Damsté, J.S., 2011. Bacterial tetraether membrane lipids in peat and coal: testing the MBT–CBT temperature proxy for climate reconstruction. Org. Geochem. 42, 477–486.
White, F., 1983. The vegetation of Africa. Natural Resources Research, UNESCO 20, 356pp.
Wright, D.K., 2017. Humans as agents in the termination of the african Humid Period. Front. Earth Sci. 5.
Yacoub, A.N., Sylvestre, F., Moussa, A., Hoelzmann, P., Alexandre, A., Dinies, M., Chalié, F., Vallet-Coulomb, C., Paillès, C., Darius, F., Sonzogni, C., Couapel, M., Mazur, J.-C., Kröpelin, S., 2023. The African Holocene Humid Period in the Tibesti mountains (central Sahara, Chad): climate reconstruction inferred from fossil diatoms and their oxygen isotope composition. Quat. Sci. Rev. 308, 108099.
Zangato, É., Holl, A.F.C., 2010. On the iron front: new evidence from north-central Africa. J. Afr. Archaeol. 8, 7–23.